

Analysis of wall-pressure fluctuation sources from DNS of turbulent channel flow

Sreevatsa Anantharamu and Krishnan Mahesh†

Aerospace Engineering and Mechanics, University of Minnesota - Twin Cities, Minneapolis, MN 55455, USA

(Received xx; revised xx; accepted xx)

The sources of wall-pressure fluctuations in turbulent channel flow are studied using a novel framework. The wall-pressure power spectral density (PSD) ($\phi_{pp}(\omega)$) is expressed as an integrated contribution from all wall-parallel plane pairs, $\phi_{pp}(\omega) = \int_{-\delta}^{+\delta} \int_{-\delta}^{+\delta} \Gamma(r, s, \omega) dr ds$, using the Green's function. Here, $\Gamma(r, s, \omega)$ is termed the net source cross spectral density (CSD) between two wall-parallel planes, $y = r$ and $y = s$ and δ is the half channel height. Direct Numerical Simulation (DNS) data at friction Reynolds number of 180 and 400 are used to compute $\Gamma(r, s, \omega)$. Analysis of the net source CSD, $\Gamma(r, s, \omega)$ reveals that the location of dominant sources responsible for the premultiplied peak in the power spectra at $\omega^+ \approx 0.35$ (Hu *et al.* 2006) and the wavenumber spectra at $\lambda^+ \approx 200$ (Panton *et al.* 2017) is in the buffer layer at $y^+ \approx 16.5$ and 18.4 for $Re_\tau = 180$ and 400, respectively. The contribution from a wall-parallel plane (located at distance y^+ from the wall) to wall-pressure PSD is log-normal in y^+ for $\omega^+ > 0.35$. A dominant inner-overlap region interaction of the sources is observed at low frequencies. Further, the decorrelated features of the wall-pressure fluctuation sources are analyzed using spectral Proper Orthogonal Decomposition (POD). Instead of the commonly used L^2 inner product, we require the modes to be orthogonal in an inner product with a symmetric positive definite kernel. Spectral POD supports the case that the net source is composed of two components - active and inactive. The dominant spectral POD mode that comprises the active part contributes to the entire wall-pressure PSD. The suboptimal spectral POD modes that constitute the inactive portion do not contribute to the PSD. Further, the active and inactive parts of the net source are decorrelated because they stem from different modes. The structure represented by the dominant POD mode at the premultiplied wall-pressure PSD peak inclines in the downstream direction. At the low-frequency linear PSD peak, the dominant mode resembles a large scale vertical pattern. Such patterns have been observed previously in the instantaneous contours of rapid pressure fluctuations by Abe *et al.* (2005).

1. Introduction

In a turbulent flow, wall-pressure fluctuations excite flexible structures. The fluctuations' spatio-temporal features determine their relation to the far-field sound radiation resulting from the structural excitation. Pressure fluctuations in an incompressible flow are governed by the Poisson equation,

$$-\frac{\partial^2 p}{\partial x_i \partial x_i} = 2\rho \frac{\partial U_i}{\partial x_j} \frac{\partial u'_j}{\partial x_i} + \rho \frac{\partial^2}{\partial x_i \partial x_j} \left(u'_i u'_j - \overline{u'_i u'_j} \right), \quad (1.1)$$

with appropriate boundary conditions. Here, p is the fluctuating pressure, ρ is the constant fluid density, and U_i and u'_i are the mean and fluctuating component of the

† Email address for correspondence: kmahesh@umn.edu

flow velocities, respectively. The linear and quadratic (in fluctuation) source terms in the above equations are called the rapid and slow terms, respectively (Pope 2001). The Poisson equation implies that the pressure fluctuation is a global quantity, meaning that the velocity at every point in the domain affects p at every point. This makes it harder to use arguments that are based on local length and velocity scale (that work reasonably well for local mean and fluctuating velocities) to analyse pressure fluctuations.

Several experiments (Willmarth & Wooldridge (1962), Corcos (1964), Blake (1970), Farabee & Casarella (1991), Gravante *et al.* (1998), Tsuji *et al.* (2007), Klewicki *et al.* (2008)) and numerical simulations (Kim (1989), Choi & Moin (1990), Kim & Hussain (1993), Chang III *et al.* (1999), Abe *et al.* (2005), Hu *et al.* (2006), Jimenez & Hoyas (2008), Sillero *et al.* (2013), Park & Moin (2016), Panton *et al.* (2017)) have studied the spatio-temporal features of wall-pressure fluctuation in turbulent boundary layer and channel flows at different Reynolds numbers. Reviews by Willmarth (1975), Bull (1996) and Blake (2017) summarize the features of wall-pressure fluctuations in wall-bounded flows.

Farabee & Casarella (1991) measured wall-pressure fluctuations in a boundary layer at friction Reynolds numbers $Re_\tau = u_\tau \delta / \nu$ ranging from 1000–2000, where $u_\tau = \sqrt{\tau_w / \rho}$ is the friction velocity, δ is the boundary layer thickness, ν is the kinematic viscosity of the fluid, τ_w is the wall-shear stress and ρ is the density of the fluid. Non-dimensionalization of the power spectral density (PSD) based on ρ, U_o and δ^* , where δ^* is the displacement thickness of the boundary layer, yielded collapse of the low frequency region ($\omega \delta / u_\tau < 5$). The mid frequency ($5 < \omega \delta / u_\tau < 100$) region showed collapse with outer flow variables (u_τ, δ, τ_w), but the high frequency region ($\omega \delta / u_\tau > 0.3 Re_\tau$) collapsed with inner flow variables (u_τ, ν, τ_w). An overlap region ($100 < \omega \delta / u_\tau < 0.3 Re_\tau$) showed collapse with both outer and inner flow variables. Based on the wall-normal location associated with the corresponding non-dimensional variable group, Farabee & Casarella (1991) hypothesized the dominant contribution to the low, mid and high frequency regions of the wall-pressure PSD to be from the unsteady potential region (above the boundary layer), outer region and inner region of the boundary layer, respectively.

Chang III *et al.* (1999) analyzed the contribution of individual source terms to wall-pressure fluctuation PSD using Green’s function formulation for $Re_\tau = 180$ channel flow. The contributions from the viscous sublayer, buffer, logarithmic and the outer region to wall-pressure fluctuation wavenumber spectra were investigated by computing partial pressures from sources located in the corresponding regions. The buffer region contribution was seen to be the most dominant for both slow and rapid terms over most of the wavenumber range. The logarithmic region was seen to contribute to the low wavenumbers through the rapid term. The viscous region was observed to contribute only to the high wavenumbers through both rapid and slow terms.

Panton *et al.* (2017) investigated wall-pressure fluctuations using DNS datasets of turbulent channel flow at Re_τ ranging from 180–5200. The premultiplied wall-pressure streamwise wavenumber spectra showed a peak around $\lambda_1^+ \approx 200 - 300$. Here, λ_1^+ is the non-dimensional streamwise wavelength based on inner units. Because the peak wavenumber scaled with inner units, Panton *et al.* (2017) believed the location of the corresponding velocity sources to be in the inner region of the channel. Further, with increasing Reynolds number, the low wavenumber contribution was observed to increase in magnitude and separate from the high wavenumber contribution. Since the dominant low wavenumbers did not scale with inner units, the corresponding velocity sources were believed to be in the outer region of the channel. Hence, the outer region contribution to wall-pressure becomes important at very high Reynolds numbers.

We investigate the decorrelated features of wall-pressure fluctuation sources in the

turbulent channel using Spectral Proper Orthogonal Decomposition (spectral POD). Spectral POD was originally introduced by Lumley (2007) and recently analyzed by Towne *et al.* (2018) for its relation to Dynamic Mode Decomposition and Resolvent analysis. It involves the eigendecomposition of the cross spectral density of the quantity of interest. The technique has been used previously (Schmidt *et al.* 2018) as a post-processing tool to infer wavepackets in axisymmetric jets. We use this technique to obtain the decorrelated contribution from each wall-parallel plane to wall-pressure fluctuation PSD. To our knowledge, this is the first work that uses spectral POD to analyze wall-pressure fluctuation sources.

Unlike the methodology of Chang III *et al.* (1999), the proposed method takes into account the wall-normal cross correlation of the source terms and accounts for the phase relationships between different wall-parallel planes. The contribution of cross-correlation between sources in any two wall-parallel planes to wall-pressure PSD is quantified as a function of frequency. Also, the collapse of the frequency and wavenumber spectrum based on inner and outer flow variables as carried out in Farabee & Casarella (1991) and Panton *et al.* (2017) do not yield such information on the wall-normal distribution, insight into which can be obtained from the proposed analysis. A ‘net source distribution function’ (also termed as ‘net source’ for brevity) is defined which yields the integrated effect of all sources in a particular wall-parallel plane. The cross spectral density (CSD) of the net source function is computed from the generated DNS database. The net source CSD when doubly integrated in the wall-normal direction yields the wall-pressure PSD and, when singly integrated yields the CSD between wall-pressure fluctuation and the net source. In addition to the spectral features, spectral POD is used to identify the decorrelated contribution from each wall-parallel plane. We present a parallel implementation of the analysis framework that is streaming, thus enabling processing of large data sets.

The paper is organized as follows. We discuss the DNS simulation details in section 2. The theory and implementation of the proposed analysis framework to investigate wall-pressure sources is discussed in sections 3.1 and 3.2, respectively. Finally, in section 4, we discuss the spectral features of the net source function, the spectral POD results and its relevance to wall-pressure fluctuation PSD using DNS data at $Re_\tau = 180$ and 400.

2. DNS simulation details

The incompressible Navier-Stokes equations are solved using the collocated finite volume method of Mahesh *et al.* (2004) in a frame of reference moving with the bulk velocity of the fluid as done by Bernardini *et al.* (2013). Better prediction of the convection velocities and high wavenumber component of the streamwise velocity fluctuations was observed by Bernardini *et al.* (2013) in the moving frame of reference. We observed a slightly better prediction of high frequency component of the wall-pressure frequency spectra with the moving frame of reference formulation. The method is second-order accurate in space. We use the Crank-Nicholson time integration scheme to ensure second-order accuracy in time and to allow for larger timesteps. The method uses a least-square cell-centred pressure gradient reconstruction to ensure discrete kinetic energy conservation in space. This ensures stability at large Reynolds number without adding numerical dissipation.

We define the subscripts x , y and z to be the streamwise, wall-normal and spanwise directions. The computational domain is a Cartesian box with side lengths $L_x = 6\pi\delta$, $L_y = 2\delta$ and $L_z = 2\pi\delta$. A long streamwise domain was chosen to include large scale contribution within the domain. Also, the long domain eliminates periodicity effects otherwise seen in low-frequency streamwise wavenumber frequency spectra (not shown). The spurious high

Re_τ	$N_x \times N_y \times N_z$	Δx^+	Δz^+	Δy_w^+	Δy_c^+	U_{bref}^+	Tu_τ/δ
180	$720 \times 176 \times 330$	4.7	3.4	0.27	4.4	15.8	8
400	$1388 \times 288 \times 660$	5.4	3.8	0.37	5.9	17.8	8

Table 1: Grid sizes, mesh spacing and velocity of the moving frame of reference used in the DNS simulation.

levels of low wavenumber region observed in the results of Choi & Moin (1990) at low frequencies is not present in the current simulation results (not shown). Table 1 shows the grid sizes (N_x, N_y, N_z) for $Re_\tau = 180$ and 400. The mesh is uniform in streamwise and spanwise directions, and a hyperbolic tangent spacing is used in the wall-normal direction with a stretching factor of 2.07 for both Re_τ . The mesh spacing in viscous units ($\Delta x^+, \Delta z^+, \Delta y_w^+, \Delta y_c^+$) is given in table 1, where $\Delta y_w^+, \Delta y_c^+$ is the wall-normal mesh spacing at the wall and at the centerline respectively. A superscript of + indicates non-dimensionalization with respect to inner layer variables u_τ and ν respectively. The resolution is sufficient enough to resolve the near wall fine scale features. The velocity of the moving frame of reference (U_{bref}^+) is chosen to be 15.8 and 17.8 for $Re_\tau = 180$ and 400 respectively. These values are close to the actual bulk velocity in the stationary frame of reference. A non-dimensional body force ($f_x \delta / \rho u_\tau^2$) of 1 is applied in the streamwise direction throughout the domain. A slip velocity equal to the negative of the frame velocity is applied at the walls. Periodic boundary conditions are used in the streamwise and spanwise directions. A timestep of $5 \times 10^{-4} \delta / u_\tau$ is used for both the simulations. The flow is initially transient and subsequently reaches a statistically stationary state when the discharge starts to oscillate around a mean value. The total simulation time for both $Re_\tau = 180$ and 400 cases is $8\delta / u_\tau$ after the initial transient period. We sample the data every timestep to compute wall-pressure statistics.

3. Analysis framework

3.1. Theory

We first write the solution to equation 1.1 using the Green's function formulation. The streamwise and spanwise extents are taken to be infinite and the frame of reference is assumed to be stationary. We use zero normal derivative of pressure fluctuation as the boundary condition at the top and bottom walls. The Stokes component of pressure arising from the non-zero wall-normal derivative of wall-pressure fluctuation at the top and bottom wall has been shown to be negligible when compared to the rapid and slow terms for high Reynolds number flows (Hoyas & Jiménez 2006; Gerolymos *et al.* 2013). The wall-normal coordinates of the top and bottom wall are $y = -\delta$ and $y = +\delta$ respectively. The Fourier transform is defined as

$$g(t) = \int_{-\infty}^{\infty} \hat{g}(\omega) e^{i\omega t} d\omega; \hat{g}(\omega) = \frac{1}{2\pi} \int_{-\infty}^{\infty} g(t) e^{-i\omega t} dt. \quad (3.1)$$

where $\hat{g}(\omega)$ is the Fourier transform of $g(t)$. The pressure fluctuation

$$\begin{aligned} p(x, y, z, t) &= \iint_{-\infty}^{\infty} \hat{p}(k_1, y, k_3, t) e^{i(k_1 x + k_3 z)} dk_1 dk_3 \\ \hat{p}(k_1, y, k_3, t) &= \int_{-\delta}^{+\delta} G(y, y', k_1, k_3) \hat{f}(k_1, y, k_3, t) dy', \\ \hat{f}(k_1, y, k_3, t) &= \frac{1}{(2\pi)^2} \iint_{-\infty}^{\infty} f(x, y, z, t) e^{-i(k_1 x + k_3 z)} dx dz, \end{aligned} \quad (3.2)$$

where $f(x, y, z, t)$ is the right hand side source term in the Poisson equation (equation 1.1), $\hat{p}(k_1, y, k_3, t)$ and $\hat{f}(k_1, y, k_3, t)$ denote the Fourier transform in the spanwise and streamwise directions of $p(x, y, z, t)$ and $f(x, y, z, t)$ respectively and the Fourier transform $\hat{p}(k_1, y, k_3, t)$ is defined similar to $\hat{f}(k_1, y, k_3, t)$ in the above equation. The Green's function $G(y, y', k_1, k_3)$ can be shown to be

$$\begin{aligned} G(y, y', k_1, k_3) &= \begin{cases} \frac{\cosh(k(y' - \delta)) \cosh(k(y + \delta))}{2k \sinh(k\delta) \cosh(k\delta)}, & y \leq y', \\ \frac{\cosh(k(y' + \delta)) \cosh(k(y - \delta))}{2k \sinh(k\delta) \cosh(k\delta)}, & y > y', \end{cases} \\ k &= \sqrt{k_1^2 + k_3^2}, \end{aligned} \quad (3.3)$$

for all combinations of k_1, k_3 except when both $k_1 = 0$ and $k_3 = 0$, for which we can obtain

$$G(y, y', k_1, k_3) = \begin{cases} \frac{1}{2}(y - y'), & y \leq y', \\ \frac{1}{2}(y' - y), & y > y'. \end{cases} \quad (3.4)$$

In order to ensure uniqueness of the Green's function when $k = 0$, we have made use of the condition that the instantaneous average of the top and bottom wall-pressure fluctuation is zero. The above Green's function has been previously used by Kim (1989) to obtain wall-pressure fluctuations from the Kim *et al.* (1987) simulation.

The wall-pressure fluctuation of a point (x, z) on the bottom wall is

$$\begin{aligned} p(x, -\delta, z, t) &= \iint_{-\infty}^{\infty} p(k_1, -\delta, k_3, t) e^{i(k_1 x + k_3 z)} dk_1 dk_3, \\ &= \iint_{-\infty}^{\infty} \int_{-\delta}^{+\delta} G(-\delta, y, k_1, k_3) f(k_1, y, k_3, t) dy e^{i(k_1 x + k_3 z)} dk_1 dk_3, \\ &= \int_{-\delta}^{+\delta} \iint_{-\infty}^{\infty} G(-\delta, y, k_1, k_3) f(k_1, y, k_3, t) e^{i(k_1 x + k_3 z)} dk_1 dk_3 dy, \\ &= \int_{-\delta}^{+\delta} f_G(x, y, z, t) dy, \end{aligned} \quad (3.5)$$

where $f_G(x, y, z, t)$ is termed as the 'net source' because it includes contribution from all sources in a wall-parallel plane and the Green's function. It includes the contribution from all streamwise and spanwise wavenumbers. The Green's function essentially assigns a weight to each wavenumber (k_1, k_3) component of the source in the wall-parallel plane. Note that the function $f_G(x, y, z, t)$ is homogenous in the streamwise and spanwise directions.

In order to characterize the features of the net source function $f_G(x, y, z, t)$, the net

source CSD $\Gamma(r, s, \omega)$ is defined as

$$\Gamma(r, s, \omega) = \frac{1}{2\pi} \int_{-\infty}^{\infty} \langle f_G^*(x, r, z, t) f_G(x, s, z, t + \tau) \rangle e^{-i\omega\tau} d\tau. \quad (3.6)$$

It can be related to the five-dimensional CSD $\varphi_{ff}(r, s, k_1, k_3, \omega)$ of the pressure Poisson source terms as

$$\Gamma(r, s, \omega) = \iint_{-\infty}^{+\infty} G^*(0, r, k_1, k_3) G(0, s, k_1, k_3) \varphi_{ff}(r, s, k_1, k_3, \omega) dk_1 dk_3, \quad (3.7)$$

where

$$\begin{aligned} \varphi_{ff}(r, s, k_1, k_3, \omega) = \\ \frac{1}{(2\pi)^3} \iiint_{-\infty}^{+\infty} \langle f^*(x, r, z, t) f(x + \xi_1, s, z + \xi_3, t + \tau) \rangle e^{-i(k_1\xi_1 + k_3\xi_3 + \omega\tau)} d\xi_1 d\xi_3 d\tau. \end{aligned} \quad (3.8)$$

The PSD of the spatially homogenous wall-pressure fluctuation $\phi_{pp}(\omega)$ is related to the net source CSD.

$$\phi_{pp}(\omega) = \int_{-\delta}^{+\delta} \int_{-\delta}^{+\delta} \Gamma(r, s, \omega) dr ds. \quad (3.9)$$

In order to analyze the contribution from a particular wall-parallel plane at $y = r$, we include its cross-correlation with every other wall-normal location $y' = s$ by integrating $\Gamma(r, s, \omega)$ along s .

$$\Psi(r, \omega) = \int_{-\delta}^{+\delta} \Gamma(r, s, \omega) ds. \quad (3.10)$$

The resulting function $\Psi(r, \omega)$ can be shown to be the CSD of the wall-pressure fluctuation and the net source at r , i.e.,

$$\Psi(r, \omega) = \frac{1}{2\pi} \int_{-\infty}^{\infty} \langle f_G^*(x, r, z, t) p(x, -1, z, t + \tau) \rangle e^{-i\omega\tau} d\tau. \quad (3.11)$$

We will call $\Psi(r, \omega)$ as the wall-pressure fluctuation - net source CSD. The wall-pressure PSD can be expressed in terms of $\Psi(r, \omega)$.

$$\phi_{pp}(\omega) = \int_{-\delta}^{+\delta} \Psi(r, \omega) dr. \quad (3.12)$$

Next, we identify decorrelated features in the dataset that contribute the most to the wall-pressure PSD using $\Gamma(r, s, \omega)$. To accomplish this, we use the Poisson inner product defined in equation 3.16 to enforce the orthonormality of the modes instead of the commonly used L^2 inner product. We decompose $\Gamma(r, s, \omega)$ as

$$\Gamma(r, s, \omega) = \sum_{i=1}^{\infty} \lambda_i(\omega) \Phi_i(r, \omega) \Phi_i^*(s, \omega), \quad (3.13)$$

where $\{\lambda_i(\omega), \Phi_i(r, \omega)\}_{i=1}^{\infty}$ are the spectral POD eigenvalue and mode pairs. The mode $\Phi_i(r, \omega)$ relates to the eigenfunction $\bar{\Phi}_i(r, \omega)$ of $\Gamma(r, s, \omega)$ through the relation

$$\Phi_i(r, \omega) = \left(-(1 - \beta) \frac{\partial^2}{\partial y^2} + \beta \right) \bar{\Phi}_i(r, \omega), \quad (3.14)$$

where β is a real number satisfying $0 < \beta \leq 1$ and the eigenfunctions are assumed to

satisfy zero Neumann boundary conditions $\bar{\Phi}_i(r, \omega)$ at $r = -\delta$ and $r = +\delta$. The eigenvalue problem for $\bar{\Phi}_i(r, \omega)$ and $\lambda_i(\omega)$ is

$$\int_{-\delta}^{+\delta} \Gamma(r, s, \omega) \bar{\Phi}_i(s, \omega) ds = \lambda_i(\omega) \left(-(1 - \beta) \frac{\partial^2}{\partial y^2} + \beta \right) \bar{\Phi}_i(r, \omega). \quad (3.15)$$

The spectral POD eigenvalues are arranged in decreasing order. The eigenfunctions $\bar{\Phi}_i(r, \omega)$ satisfy the orthonormality condition

$$\begin{aligned} &= \int_{-\delta}^{+\delta} \bar{\Phi}_i^*(r, \omega) \left(-(1 - \beta) \frac{\partial^2}{\partial y^2} + \beta \right) \bar{\Phi}_j(r, \omega) dr \\ &= \delta_{ij}, \end{aligned} \quad (3.16)$$

where δ_{ij} is the Kroenecker delta. We will call the inner product above ‘the Poisson inner product’ because the kernel $\left(-(1 - \beta) \frac{\partial^2}{\partial y^2} + \beta \right)$ can be related to the Poisson equation. If we choose $\beta = 1$, then the Poisson inner product is the standard L^2 inner product.

The contribution of each spectral POD mode to wall-pressure PSD can be obtained by integrating equation 3.13 in r and s ,

$$\phi_{pp}(\omega) = \sum_{i=1}^{\infty} \gamma_i(\omega); \quad \gamma_i(\omega) = \lambda_i(\omega) \left| \int_{-\delta}^{+\delta} \Phi_i(r, \omega) dr \right|^2; \quad i = 1, \dots, \infty. \quad (3.17)$$

In the above equation, the wall-pressure PSD is expressed as sum of positive contributions $\{\gamma_i(\omega)\}_{i=1}^{\infty}$ from each spectral POD mode. We will use the quantities $\{\gamma_i(\omega)\}_{i=1}^{\infty}$ to identify the spectral POD modes that are the dominant contributors to wall-pressure PSD.

The spectral POD modes and eigenvalues depend on the parameter β . For a chosen value of β , we will have the corresponding set of spectral POD modes $\{\Phi_i(y, \omega)\}_{i=1}^{\infty}$ and eigenvalues $\{\lambda_i(\omega)\}_{i=1}^{\infty}$. However, irrespective of the chosen β , the component of the net source Fourier transform ($\hat{f}_G(x, y, z, \omega)$) along the spectral POD modes will be decorrelated, i.e.,

$$\begin{aligned} f_G(x, y, z, t) &= \int_{-\infty}^{+\infty} \hat{f}_G(x, y, z, \omega) e^{i\omega t} d\omega, \\ \hat{f}_G(x, y, z, \omega) &= \sum_{j=1}^{\infty} \alpha_j(x, z, \omega) \Phi_j^*(y, \omega), \end{aligned} \quad (3.18)$$

$$\langle \alpha_i(x, z, \omega) \alpha_j^*(x, z, \omega_o) \rangle = \lambda_i(\omega) \delta_{ij} \delta(\omega - \omega_o),$$

where $\{\alpha_j(x, z, \omega)\}_{j=1}^{\infty}$ are the coefficients, $\langle \cdot \rangle$ denotes ensemble average and δ is the Dirac delta function.

On the other hand, choosing the L^2 inner product ($\beta = 1$) to enforce the orthonormality of the modes will also optimally decompose the wall-normal integral of the PSD $\Gamma(r, r, \omega)$. Substituting $s = r$ in equation 3.13 and integrating in r , we obtain

$$\begin{aligned} \Gamma(r, r, \omega) &= \sum_{j=1}^{\infty} \lambda_j(\omega) |\Phi_j(r, \omega)|^2, \\ \int_{-\delta}^{+\delta} \Gamma(r, r, \omega) dr &= \sum_{j=1}^{\infty} \lambda_j(\omega). \end{aligned} \quad (3.19)$$

However, the dominant spectral POD modes obtained with the L^2 inner product do

not necessarily isolate the main contribution to the wall-pressure PSD. i.e., the value of $\gamma_i(\omega)$. That is, the wall-pressure PSD can be distributed over a large number of modes that each individually contribute a small fraction. This makes it difficult to identify the few dominant decorrelated source patterns. Further, the single dominant wall-pressure mode (mode with largest $\gamma_i(\omega)$) does not necessarily contain any useful information about the source because it contributes only a small fraction to the wall-pressure PSD. This was observed at low frequencies (see figure 16).

Our goal is to identify useful decorrelated features of the wall pressure source, not to optimally decompose the integrated net source PSD (as done by the L^2 inner product). Therefore, we use the parameter β to our advantage and select a suitable value for β .

For $0 < \beta < 1$, it can be shown that the Poisson inner product optimally decomposes $\iint_{-\delta}^{+\delta} G(s, r, \beta/(1-\beta), 0)/(1-\beta)\Gamma(r, s, \omega) dr ds$ into the sum of spectral POD eigenvalues,

$$\iint_{-\delta}^{+\delta} \frac{G(s, r, \frac{\beta}{1-\beta}, 0)}{1-\beta} \Gamma(r, s, \omega) dr ds = \sum_{j=1}^{\infty} \lambda_j(\omega), \quad (3.20)$$

where the Green's function G is given in equation 3.3. We can observe that as β approaches 0, the Green's function $G(r, s, \beta/(1-\beta), 0)$ becomes flatter and approaches a function that is constant in r and s . Thus, the left hand side in the above equation approaches the wall-pressure PSD $\phi_{pp}(\omega) = \iint_{-1}^{+1} \Gamma(r, s, \omega) dr ds$ (up to a scaling). As we decrease β , we can therefore expect the dominant spectral POD modes to be the dominant contributors to wall-pressure PSD. Therefore, the Poisson inner product in equation 3.16 identifies the few dominant features of wall-pressure sources that are decorrelated.

The Poisson inner product defined in equation 3.16 does not fall into the category presented by Towne *et al.* (2018). They require the eigenfunctions to be orthonormal in a weighted L^2 inner product. Here, we use the Poisson inner product (3.16) that has a symmetric positive definite kernel.

The set of spectral POD modes obtained with any β is complete. Therefore, we can relate the POD modes obtained with two different values of β to each other through a linear transformation. That is, if $\{\hat{\Phi}_i(y, \omega)\}_{i=1}^{\infty}$ and $\{\tilde{\Phi}_i(y, \omega)\}_{i=1}^{\infty}$ are the two sets of spectral POD modes obtained with two different values of β , then

$$\hat{\Phi}_i(y, \omega) = \sum_j C_{ij}^*(\omega) \tilde{\Phi}_j(y, \omega), \quad (3.21)$$

where the matrix $C(\omega) = [C_{ij}(\omega)]$ is the linear transformation. Further, we show in Appendix B that the linear transformation $C(\omega)$ is indeed orthogonal with an appropriate row scaling, i.e.,

$$\left(\hat{\Lambda}^{1/2}(\omega)C(\omega)\right)^H \hat{\Lambda}^{1/2}(\omega)C(\omega) = \tilde{\Lambda}(\omega), \quad (3.22)$$

where $\hat{\Lambda}(\omega)$ and $\tilde{\Lambda}(\omega)$ are the diagonal matrices of eigenvalues of the set of modes $\{\hat{\Phi}_i(y, \omega)\}_{i=1}^{\infty}$ and $\{\tilde{\Phi}_i(y, \omega)\}_{i=1}^{\infty}$, respectively.

We can show that

$$\left| \int_{-\delta}^{+\delta} \Phi_i(y, \omega) dy \right| = \int_{-\delta}^{+\delta} |\Phi_i(y, \omega)| \cos(\angle \Phi_i(y, \omega) - \angle \Phi_i^n(\omega)) dy, \quad (3.23)$$

where $\angle \Phi_i^n(\omega) = \angle \left(\int_{-\delta}^{+\delta} \Phi_i(y, \omega) dy \right)$ and \angle denotes the phase of the complex number

that follows it. Using equation 3.23 in equation 3.17, we obtain

$$\gamma_i(\omega) = \lambda_i(\omega) \left(\int_{-\delta}^{+\delta} |\Phi_i(r, \omega)| \cos(\angle \Phi_i(r, \omega) - \angle \Phi_i^n(\omega)) dr \right)^2; i = 1, \dots, \infty. \quad (3.24)$$

From the above equation, we can observe that the eigenvalue, magnitude and phase of the spectral POD mode, all play a role in determining its contribution to wall-pressure PSD. Sources contained in wall-normal regions where the phase is in the range $|\angle \Phi_i(y, \omega) - \angle \Phi_i^n(\omega)| < \pi/2$ undergo destructive interference with the sources contained in the region where $\pi/2 < |\angle \Phi_i(y, \omega) - \angle \Phi_i^n(\omega)| < \pi$. Therefore, the interference of the sources from different wall-normal regions represented by a spectral POD mode plays a role in determining the net contribution to wall-pressure PSD from the mode.

3.2. Implementation

The five-dimensional CSD $\varphi_{ff}(r, s, k_1, k_3, \omega)$ defined in equation 3.8 contains all pertinent information on velocity field sources from cross-correlation of two wall-normal locations. However, computing the function is extremely memory intensive. For the $Re_\tau = 400$ case, assuming 2000 frequencies, we would need $\approx 1220TB$ to store φ_{ff} . We use a streaming parallel implementation procedure to compute the net source CSD $\Gamma(r, s, \omega)$ that makes the computation feasible.

The source term in equation 1.1 is computed and stoblack from the DNS. The stoblack data is divided into multiple chunks to compute the ensemble average in equation 3.8. For a given chunk, the source terms are first converted to stationary frame of reference and then Fourier transformed in x , z and t . The Fourier transforms are then used to update the net source CSD. Details of the parallel implementation are provided in the Appendix.

A total of 16000 timesteps are used to obtain the net source CSD $\Gamma(r, s, \omega)$ for both Re_τ . We sample the data ever timestep. The number of timesteps in each chunk is 2000 and 50% overlap is used in time to increase statistical convergence. The frequency resolution of the analysis is $\Delta\omega\delta/u_\tau = 2\pi$.

4. Results and discussion

First, we discuss the spectral features of the wall-pressure fluctuations obtained from the finite volume solver. Then, the wall pressure net source cross spectral density (wall-pressure fluctuation - net source CSD) and the dominant decorrelated net source patterns obtained using spectral POD are discussed. For validation of the current DNS, we refer the reader to appendix C.

4.1. DNS wall-pressure fluctuations

The one-sided PSD of the obtained $Re_\tau = 180$ and 400 wall-pressure fluctuations scaled with inner variables is shown in figure 1a. The streamwise wavenumber spectra of the fluctuations at the two Re_τ are shown in figure 2a. Both the PSD and wavenumber spectra at $Re_\tau = 180$ agree well with the results of Choi & Moin (1990). The high frequency region with $\omega^+ = \omega\nu/u_\tau^2 > 1$, shows a small region of -5 decay for the higher Reynolds number ($Re_\tau = 400$). The high wavenumber region of the wavenumber spectra plotted in figure 2a also shows a small region of -5 decay in the region $k_1^+ = k_1\nu/u_\tau > 0.1$, for the $Re_\tau = 400$ case. The premultiplied power spectra plotted in figure 1b for both Re_τ shows a peak at $\omega_p^+ = 0.35$. This peak at the same frequency has been previously observed by Hu *et al.* (2006) for Re_τ upto 1440. Similar to the power spectra, the premultiplied streamwise

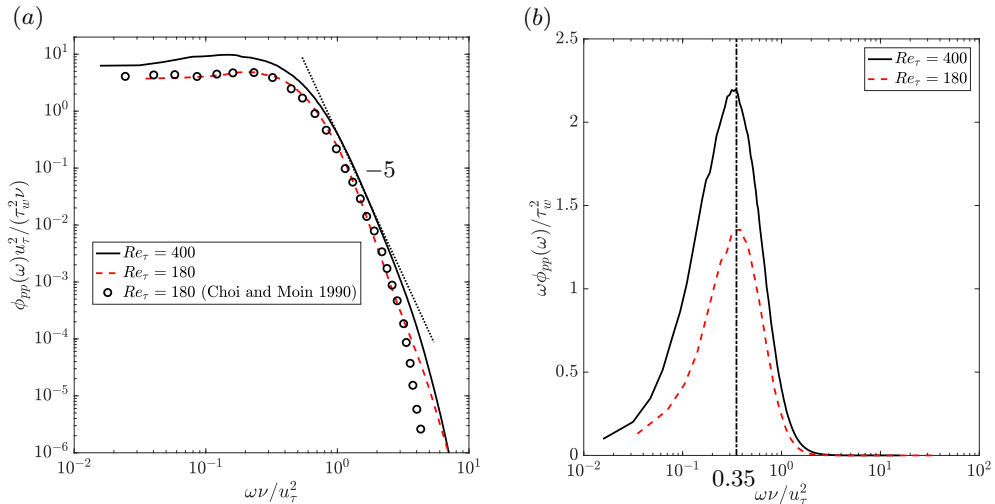


Figure 1: Wall-pressure fluctuation power spectra in (a) inner units (b) premultiplied form with inner units on x-axis.

wavenumber spectra in figure 2b also shows a peak at $k_1^+ = k_1 \nu / u_\tau$ at $k_p^+ = 0.027$. This peak has also been previously observed by Panton *et al.* (2017) for Re_τ over the range 180 to 5000. The wall-pressure fluctuation PSD computed from the net source CSD using equation 3.9 agrees with that obtained directly from the solver (figure 1a) for both Re_τ (not shown). We will investigate the distribution of the net sources that give rise to this premultiplied PSD peak in the next section.

To identify the range of -5 decay in the power and streamwise wavenumber spectrum, we plot the diagnostic functions $(\omega \nu / u_\tau^2)^5 \phi_{pp}(\omega) u_\tau^2 / (\tau_w^2 \nu)$ and $(k_1 \nu / u_\tau)^5 \phi_{pp}(k_1) u_\tau / (\tau_w^2 \nu)$ in figures 3a and b, respectively. The function is constant in the range of -5 slope. The diagnostic function does not return a significant range of frequency and wavenumbers that show -5 decay. We observe a constant value (indicated by dashed-dotted horizontal line) for only a very small range of frequencies and wavenumbers. To observe the decay in a significant range, we require higher Reynolds numbers.

The wall-pressure wavenumber spectra shows a low wavenumber peak around $k_1 \delta \approx 3$ for both $Re_\tau = 180$ and 400, respectively when the y-axis is plotted in linear coordinates (figure 4a). This corresponds to streamwise wavelengths λ_1 / δ of ~ 2 . Such low wavenumber peaks in the range $k_x \delta \approx 2.5 - 3.4$ ($\lambda_x / \delta \approx 1.8 - 2.4$) have been previously observed by Abe *et al.* (2005) and Panton *et al.* (2017) in turbulent channel for friction Reynolds numbers ranging from 180 to 5000. We observe the corresponding low frequency peak in the wall-pressure PSD at $\omega \delta / u_\tau = 37.6$ and 50.2 for $Re_\tau = 180$ and 400, respectively (shown in figure 4b). Later, we identify the decorrelated fluid sources responsible for this low frequency peak in the PSD using spectral POD and relate to the observations of Abe *et al.* (2005).

Figure 4c shows the spanwise wavenumber spectrum of the wall-pressure fluctuations in inner units. The spectrum at $Re_\tau = 180$ agrees well with Choi & Moin (1990). Therefore, the spanwise resolution is sufficient enough to resolve the fine scale spanwise features of wall-pressure fluctuations.

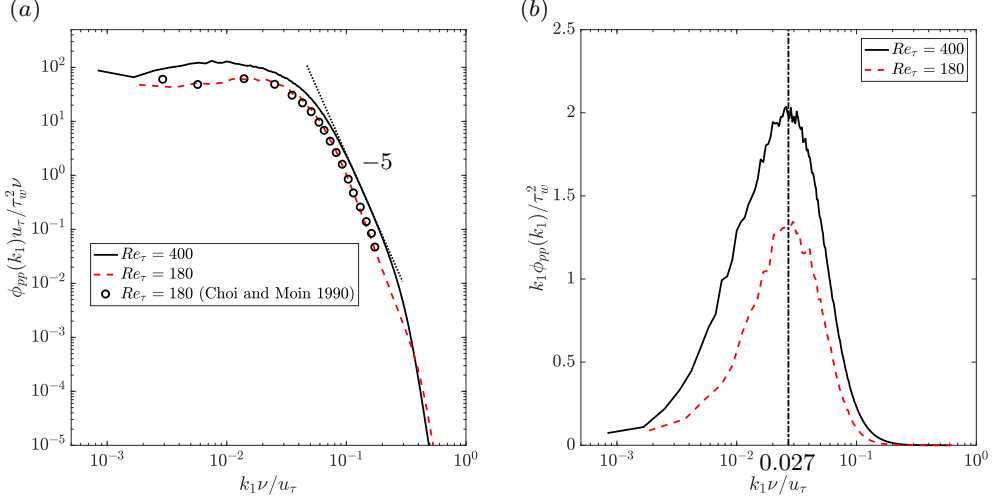


Figure 2: Wall-pressure fluctuation streamwise wavenumber spectra in (a) inner units (b) pre-multiplied form with inner units on x-axis.

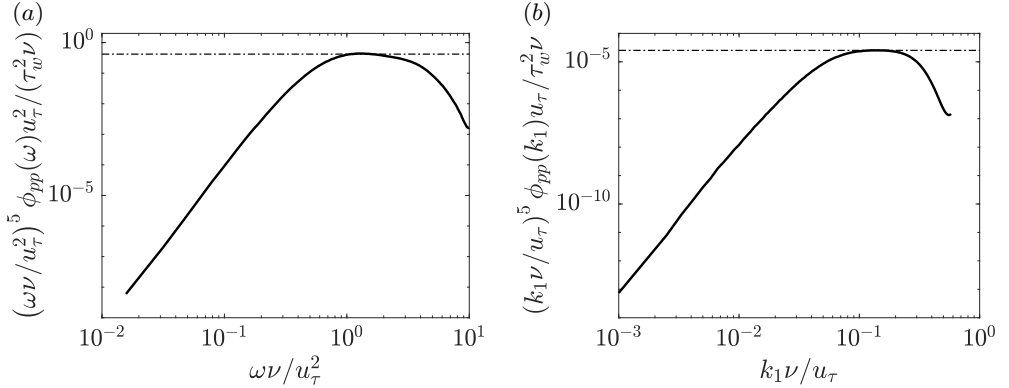


Figure 3: Diagnostic function to verify region of -5 slope in the $Re_\tau = 400$ a) power and b) streamwise wavenumber spectrum. The dashed-dotted horizontal line in figures a and b indicates constant values of 0.42 and 2.53×10^{-5} , respectively.

4.2. Wall-pressure source distribution analysis

The wall-parallel plane that contributes the most to the wall-pressure PSD can be determined from the real part of the wall-pressure fluctuation - net source CSD $\Psi(y^+, \omega^+)$ (defined in section 3.1). Figure 5a shows the wall-pressure fluctuation - net source CSD in pre-multiplied form normalized by the root mean square (RMS) of the wall-pressure fluctuations $(y^+ \omega^+ Re(\Psi^+(y^+, \omega^+))/\langle p^2 \rangle^+)$. y^+ is the distance from the wall in viscous units. The coordinates (ω_p^+, y_p^+) of the peak value in the contours occur at $(0.35, 16.5)$ and $(0.35, 18.4)$ for $Re_\tau = 180$ and 400 , respectively. The frequency coordinate of the peak in the contour levels ($\omega^+ = 0.35$) is same as the pre-multiplied power spectra peak location shown in figure 1b. Therefore, the corresponding wall-normal coordinate yields the location of the wall-parallel plane that contributes the most to the pre-multiplied power spectra peak. Specifically, it is the cross-correlations with this dominant plane that contributes the most. This coincidence is not surprising since integrating figure 5a

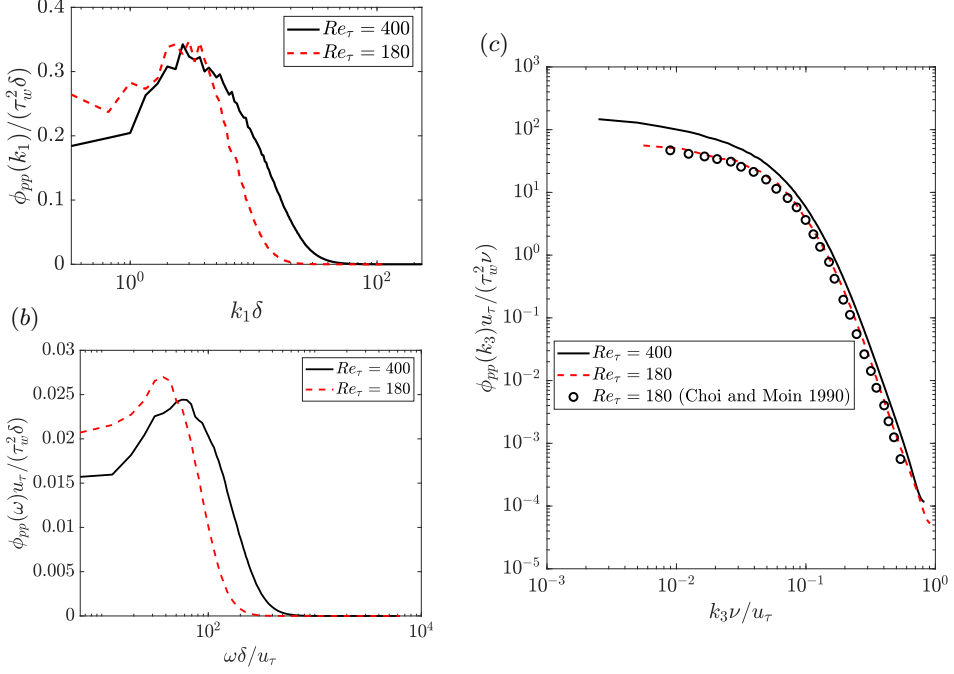


Figure 4: (a) Wall-pressure fluctuation streamwise wavenumber spectrum with linear y-axis. (b) Wall-pressure fluctuation PSD with linear y-axis. (c) Wall-pressure fluctuation spanwise wavenumber spectrum in inner units.

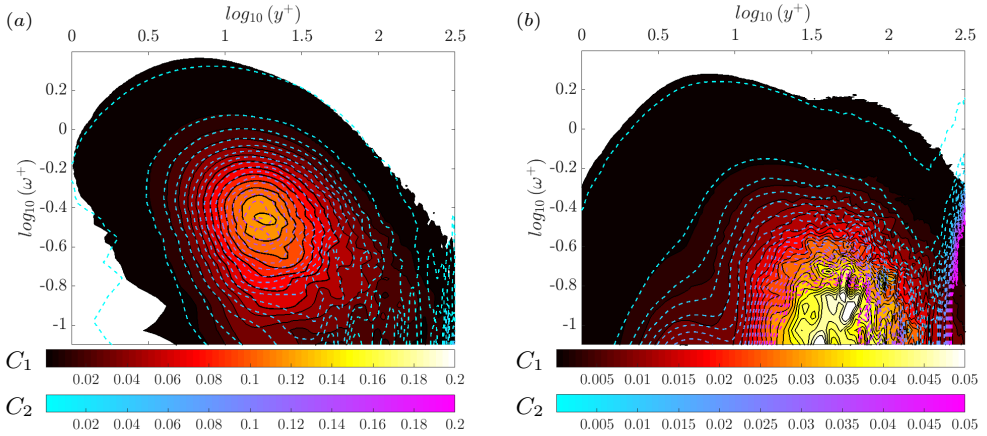


Figure 5: a) Real part of premultiplied wall-pressure fluctuation - net source CSD $(y^+ \omega^+ Re(\Psi(y^+, \omega^+))/\langle p^2 \rangle)$ for $Re_\tau = 400$ (black solid lines with filled contours with colormap C_1) and 180 (line contours with colormap C_2). Contour lines are 20 equally spaced values between $4e-4$ and $2e-1$. b) Premultiplied net source PSD $(y^+ \omega^+ \Gamma(y^+, \omega^+)/\langle \Gamma^2 \rangle)$ for $Re_\tau = 400$ (black solid lines with filled contours with colormap C_1) and 180 (line contours with colormap C_2). Contour lines are 20 equally spaced values between $4e-5$ and $5e-2$

in wall-normal direction yields figure 1b (normalized by $\langle p^2 \rangle$). The wall-normal coordinate of the peak indicates that it is the correlations with the buffer region that contribute the most to the wall-pressure PSD at the Reynolds numbers considered.

Even though the peak location differs slightly in inner units for the two Re_τ , the main implication of this result is that the peak lies in the buffer region. Further, we cannot expect the same location of the peak for both Re_τ . This is because the real part of the peak wall-pressure fluctuation - net source CSD includes the contribution from the correlations with the rest of the channel (since $\Psi(y_p^+, \omega) = \int_{-\delta}^{+\delta} \Gamma(y_p^+, y', \omega) dy'$) and not just the inner layer. Therefore, the peak need not necessarily scale in inner units. We believe that changing the Reynolds number would not affect this main finding. We expect the peak value of wall-pressure fluctuation - net source CSD to still occur in the buffer layer.

The phase difference between the wall-pressure and the dominant net source obtained from the argument of $\Psi(y_p^+, \omega_p^+)$ is 0.013π and 0.016π for $Re_\tau = 180$ and 400 respectively, is very small. Hence, the dominant net sources and the wall-pressure fluctuation are in phase with each other. The contour levels of the normalized wall-pressure fluctuation - net source CSD plotted in figure 5a almost overlap in the range $\omega^+ > 0.3 \sim 10^{-0.5}$. This indicates that the high frequency contribution to the RMS scales in inner units. However, in the near wall region ($y^+ < 10$), the overlap in the contours is observed for a much larger frequency range $\omega^+ > 0.16 \sim 10^{-0.8}$. This implies that for most of the frequency range, the contribution to wall-pressure PSD from the near-wall region scales in inner units.

Next, we investigate whether the net source PSD can be used to infer the location of the dominant source of wall-pressure fluctuation instead of the wall-pressure fluctuation - net source CSD. Figure 5b shows the contours of the premultiplied net source PSD $\Gamma(y^+, y^+, \omega^+)$ in fractional form for both Re_τ . The main contribution to the net source PSD is seen to be from the region around $y^+ \approx 30$ and at frequencies much lower than $\omega^+ \approx 0.35$. There is no signature of the distinct premultiplied peak observed in figure 5a. From visual inspection at low frequencies ($\omega^+ < 1$), the shape of the contours in figure 5b do not have similar shape to those in figure 5a. However, at high frequencies $\omega^+ > 1$, we observe from figure 6a and 6b that the contour shapes near the wall ($y^+ < 30$) are almost identical. Therefore, the net source PSD $\Gamma(y^+, y^+, \omega^+)$ is a good proxy for wall-pressure fluctuation - net source CSD $\Psi(y^+, \omega^+)$ at high frequencies to obtain the pattern of the net sources. The reason for this behavior can be understood from the near wall contours of the real part of the net source CSD shown in figure 7. Figures 7a and 7b show the contours at frequencies $\omega^+ = 0.35$ and $\omega^+ = 1$, respectively for $Re_\tau = 180$. Clearly, the low frequency ($\omega^+ = 0.35$) contours show a large negatively cross correlated region around $(y^+, y'^+) = (5, 15)$ (shown by white boxes). These dominant negative regions found at low frequencies contribute to the wall-pressure fluctuation - net source CSD (equation 3.10) leading to different shapes compared to net source PSD. However, such negative regions are not present at the higher frequency $\omega^+ = 1$. Therefore, the wall-pressure fluctuation - net source CSD and the net source CSD have similar shapes near to the wall at high frequencies.

The wall-pressure fluctuation - net source CSD (normalized with wall-pressure PSD) is plotted in premultiplied form for selected frequencies between $\omega^+ = 0.35$ and $\omega^+ = 2$ in figure 8a. Due to the normalization, each profile has unit area under it. From the figure, we can observe that the curves for $Re_\tau = 180$ and 400 are very close to each other for the different frequencies plotted. Further, visual inspection shows that we can model the profiles using log-normal function in y^+ . Therefore, normalized log-normal profiles of the

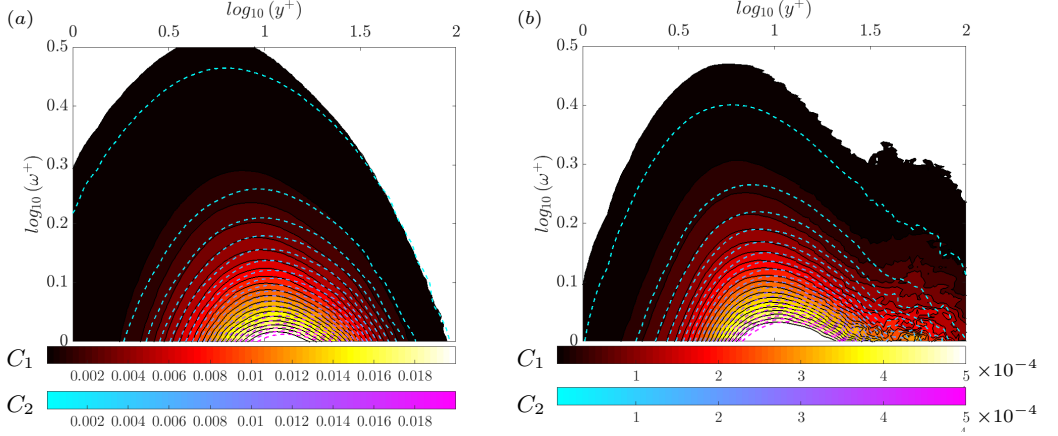


Figure 6: a) Real part of the high frequency premultiplied wall-pressure fluctuation - net source CSD ($y^+\omega^+Re(\Psi(y^+, \omega^+))/\langle p^2 \rangle$) for $Re_\tau = 400$ (black solid lines with filled contours with colormap C_1) and 180 (line contours with colormap C_2). Contour lines are 20 equally spaced values between $4e-5$ and $2e-2$. b) High frequency premultiplied fractional net source power spectral density $y^+\omega^+\Gamma(y^+, y^+, \omega^+)/\langle \Gamma^2 \rangle$ for $Re_\tau = 400$ (black solid lines with filled contours with colormap C_1) and 180 (line contours with colormap C_2). Contour lines are 20 equally spaced values between $4e-6$ and $2e-2$

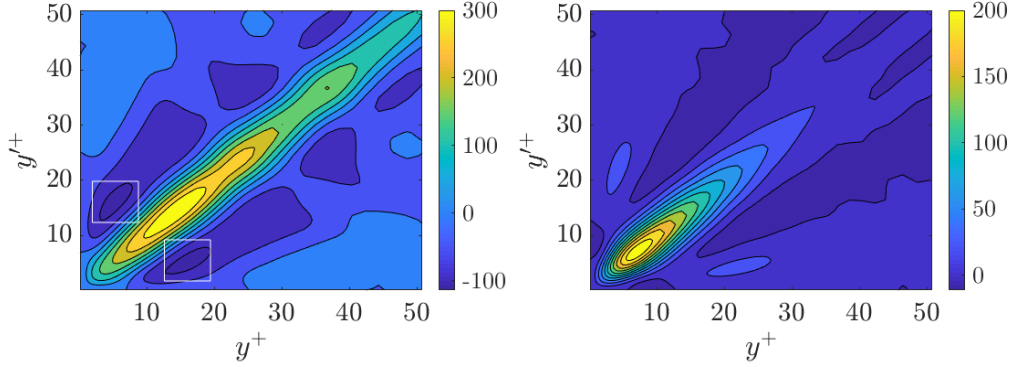


Figure 7: Real part of $\Gamma(r, s, \omega)$ (normalized by $\phi_{pp}(\omega)$) at a) $\omega^+ \approx 0.35$ and b) $\omega^+ \approx 1$ for $Re_\tau = 180$.

form

$$f(y^+, \omega^+) = \frac{1}{\sigma(\omega^+) \sqrt{2\pi}} \exp \left(- \left(\frac{\ln(y^+) - \mu(\omega^+)}{\sqrt{2}\sigma(\omega^+)} \right)^2 \right) \quad (4.1)$$

are fitted to the $Re_\tau = 400$ data for different ω^+ using nonlinear least squares fit and plotted in figure 8b.

The mean and standard deviation of the fitted log-normal curves characterize the location and the width of the dominant net source respectively as a function of frequency. The correlation between the planes contained in this width have a sizeable contribution to wall-pressure PSD. Figure 8c and 8d show the mean ($\mu(\omega^+)$) and standard deviation ($\sigma(\omega^+)$) as a function of frequency respectively. We define the location of the dominant

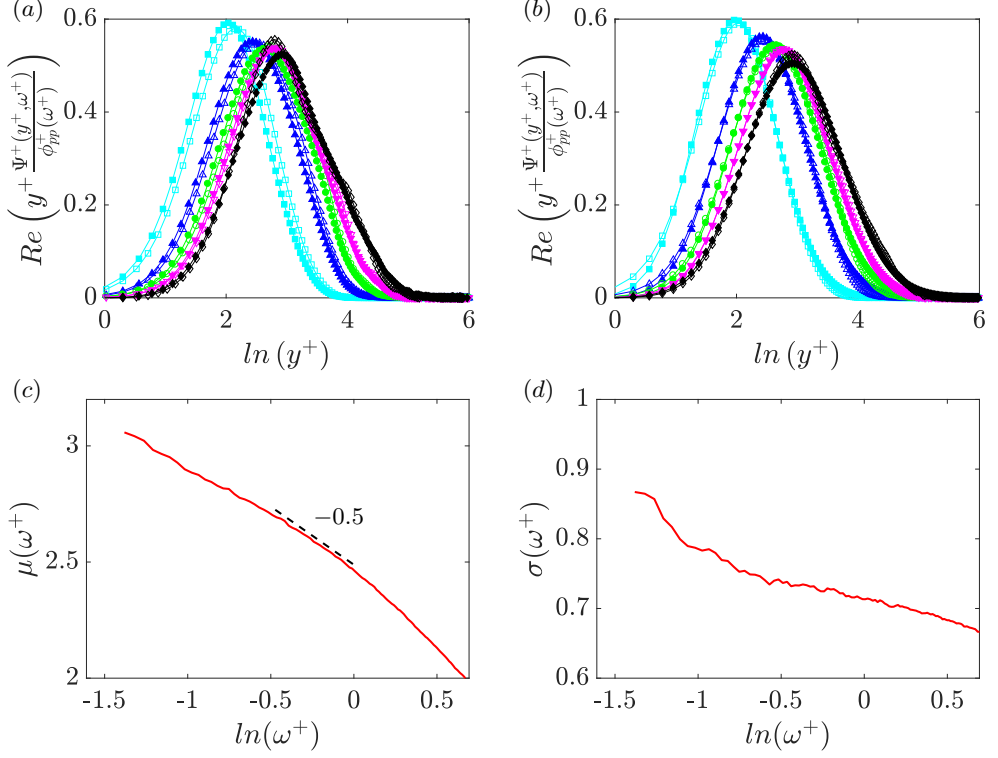


Figure 8: a) Premultiplied wall-pressure fluctuation - net source CSD $(y^+ \Psi^+(y^+, \omega^+)/\phi_{pp}^+(\omega^+))$ at different frequencies for $Re_\tau = 180$ (empty markers) and 400 (filled markers). b) Comparison of fitted log-normal Gaussians (filled markers) to the wall-pressure fluctuation - net source for $Re_\tau = 400$ (empty markers). c) Variation of mean $\mu(\omega^+)$ and d) standard deviation $\sigma(\omega^+)$ of the fitted log-normal profile for $Re_\tau = 400$. \diamond, \blacklozenge : $\omega^+ \approx 0.35$, $\nabla, \blacktriangledown$: $\omega^+ \approx 0.5$, \circ, \bullet : $\omega^+ \approx 0.7$, $\triangle, \blacktriangle$: $\omega^+ \approx 1$, \square, \blacksquare : $\omega^+ \approx 2$.

net source $y_p^+(\omega^+)$ as $y_p^+(\omega^+) = \exp(\mu(\omega^+))$. From figure 8c, we observe that the location of the dominant net source moves closer to the wall with increase in frequency through a power law dependence $y_p^+ \sim (\omega^+)^m$. The value of m depends on the frequency range. In the low $(-1.5 < \ln(\omega^+) < 0.5)$, mid $(-0.5 < \ln(\omega^+) < 0)$ and high $(\omega^+ > 1)$ frequency range, the value of the exponent m is larger than -0.5 , equal to -0.5 and smaller than -0.5 respectively.

Figure 8d shows that the standard deviation of the log-normal profiles decreases with increasing frequency. We use the standard deviation profile to show that for $\omega^+ > e^{-1}$, the width of the dominant net source is proportional to its location. We define the wall-normal width of the net source $\Delta y^+(\omega^+; \alpha, \sigma)$ as

$$\Delta y^+(\omega^+; \alpha, \sigma) = y_{max}^+(\omega^+; \alpha, \sigma) - y_{min}^+(\omega^+; \alpha, \sigma), \quad (4.2)$$

where y_{max}^+, y_{min}^+ and y_p^+ are related as

$$\begin{aligned} \ln(y_{max}^+(\omega^+; \alpha, \sigma)) - \ln(y_{min}^+(\omega^+; \alpha, \sigma)) &= 2\alpha\sigma(\omega^+), \\ \ln(y_p^+(\omega^+)) - \ln(y_{min}^+(\omega^+; \alpha, \sigma)) &= \alpha\sigma(\omega^+). \end{aligned} \quad (4.3)$$

The parameter α is the proportion of the standard deviation used to define the width of

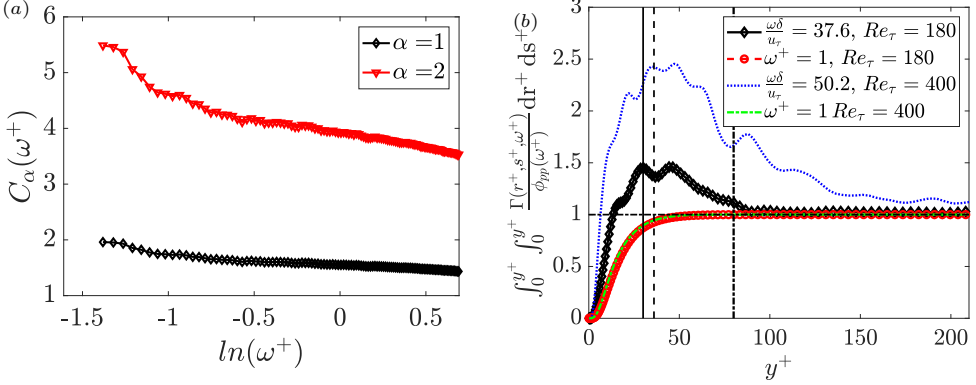


Figure 9: a) Variation of $C_\alpha(\omega^+)$ for $Re_\tau = 400$. b) Partial wall-pressure fluctuation spectra from sources that extend from the wall to a particular y^+ for $Re_\tau = 180$ and 400 in near wall region. The vertical solid, dashed, dash-dotted lines denote $y^+ = 30$, $y/\delta = 0.2$ for $Re_\tau = 180$ and $y/\delta = 0.2$ for $Re_\tau = 400$, respectively. The horizontal dash-dotted line denotes partial contribution equal to 1.

the net source. Using the above expressions, the width $\Delta y^+(\omega^+; \alpha, \sigma)$ can be shown to be

$$\begin{aligned} \Delta y^+(\omega^+; \alpha, \sigma) &= C(\omega^+; \alpha, \sigma) y_p^+(\omega^+), \\ C(\omega^+; \alpha, \sigma) &= \left(e^{\alpha\sigma(\omega^+)} - e^{-\alpha\sigma(\omega^+)} \right). \end{aligned} \quad (4.4)$$

The variation of $C_\alpha(\omega^+)$ for $\alpha = 1, 2$ using $Re_\tau = 400$ data is shown in figure 9a. The proportionality constant is observed to vary slowly for $\omega^+ > \ln(-1)$. Hence, in this frequency range, the width of the dominant net source is proportional to its location.

The contribution of the interaction between the net sources in the inner and overlap/outer region to wall-pressure PSD can be investigated using the wall-pressure fluctuation - net source CSD. Figure 9b shows the partial contribution (normalized by the wall-pressure PSD) $\int_0^{y^+} \int_0^{y^+} \frac{\Gamma(r^+, s^+, \omega^+)}{\phi_{pp}(\omega^+)} dr^+ ds^+$ from the net sources contained between the wall and a given y^+ for two selected frequencies. At the low frequency wall-pressure linear PSD peak (which is $\omega\delta/u_\tau = 37.6$ and $\omega\delta/u_\tau = 50.2$ for $Re_\tau = 180$ and 400 , respectively), we observe that the partial contribution first increases and then decreases. However, a monotonically increasing behavior is observed for the high frequency. In order to investigate the implication of the non-monotonic low frequency behavior, we split the domain $0 < y/\delta < 1$ into an inner region $0 < y^+ < 30$, an outer/overlap region $30 < y^+ < Re_\tau$. The contribution to wall-pressure PSD from sources within $y/\delta = 1$ can then be accordingly split as

$$\begin{aligned} \int_0^{Re_\tau} \int_0^{Re_\tau} \frac{\Gamma(r^+, s^+, \omega^+)}{\phi_{pp}(\omega^+)} dr^+ ds^+ &= \int_0^{30} \int_0^{30} \frac{\Gamma(r^+, s^+, \omega^+)}{\phi_{pp}(\omega^+)} dr^+ ds^+ + \\ &\quad \int_{30}^{Re_\tau} \int_{30}^{Re_\tau} \frac{\Gamma(r^+, s^+, \omega^+)}{\phi_{pp}(\omega^+)} dr^+ ds^+ + \\ &\quad 2Re \left(\int_0^{30} \int_{30}^{Re_\tau} \frac{\Gamma(r^+, s^+, \omega^+)}{\phi_{pp}(\omega^+)} dr^+ ds^+ \right). \end{aligned} \quad (4.5)$$

From figure 9b, we observe that at the lower frequency, this contribution from sources

within $y/\delta = 1$ is smaller than the inner region contribution $\int_0^{30} \int_0^{30} \frac{\Gamma(r^+, s^+, \omega^+)}{\phi_{pp}(\omega^+)} dr^+ ds^+$. Therefore,

$$\int_0^{Re_\tau} \int_0^{Re_\tau} \frac{\Gamma(r^+, s^+, \omega^+)}{\phi_{pp}(\omega^+)} dr^+ ds^+ \leq -2Re \left(\int_0^{30} \int_0^{Re_\tau} \frac{\Gamma(r^+, s^+, \omega^+)}{\phi_{pp}(\omega^+)} dr^+ ds^+ \right). \quad (4.6)$$

Note the the left hand side of the above inequality is a positive real number. This indicates that i) the contribution from the cross-correlations between the inner and the overlap/outer region dominantes the contribution from the outer/overlap region alone, ii) the phase difference between the net sources in these two regions is pblackominantly in the range $\pi/2$ to π or $-\pi$ to $-\pi/2$. In other words, a positive (or negative) low frequency event in the near-wall region is pblackominantly correlated with a negative (or positive) low frequency event in the overlap/outer region. Therefore, the observed non-monotonic behavior at low frequencies implies a dominant interaction between the net sources the inner and outer regions of the channel at such frequencies. Such inner-outer interaction at long streamwise wavelengths has been previously observed for the streamwise velocity fluctuations by Del Álamo & Jiménez (2003), Morrison (2007), and is the reason for the mixed scaling (De Graaff & Eaton 2000) of the streamwise velocity RMS peak in wall-bounded flows.

We further investigate the fractional contribution of the wall-pressure sources in the inner ($y^+ < 30$), overlap ($30 < y^+ < 0.2Re_\tau$) and outer region ($0.2 < y/\delta < 1$) and their cross-correlations to the wall-pressure PSD by splitting $\int_0^{Re_\tau} \int_0^{Re_\tau} \frac{\Gamma(r^+, s^+, \omega^+)}{\phi_{pp}(\omega^+)} dr^+ ds^+$ into the sum,

$$\begin{aligned} & \int_0^{Re_\tau} \int_0^{Re_\tau} \frac{\Gamma(r^+, s^+, \omega^+)}{\phi_{pp}(\omega^+)} dr^+ ds^+ = \\ & \underbrace{\int_0^{30} \int_0^{30} \frac{\Gamma(r^+, s^+, \omega^+)}{\phi_{pp}(\omega^+)} dr^+ ds^+}_{C_{11}} + \\ & \underbrace{\int_0^{0.2Re_\tau} \int_0^{0.2Re_\tau} \frac{\Gamma(r^+, s^+, \omega^+)}{\phi_{pp}(\omega^+)} dr^+ ds^+}_{C_{22}} + \underbrace{\int_0^{Re_\tau} \int_0^{Re_\tau} \frac{\Gamma(r^+, s^+, \omega^+)}{\phi_{pp}(\omega^+)} dr^+ ds^+}_{C_{33}} + \\ & 2Re \left(\underbrace{\int_0^{30} \int_0^{0.2Re_\tau} \frac{\Gamma(r^+, s^+, \omega^+)}{\phi_{pp}(\omega^+)} dr^+ ds^+}_{C_{12}} + \underbrace{\int_0^{0.2Re_\tau} \int_0^{Re_\tau} \frac{\Gamma(r^+, s^+, \omega^+)}{\phi_{pp}(\omega^+)} dr^+ ds^+}_{C_{23}} + \right. \\ & \left. \underbrace{\int_0^{Re_\tau} \int_0^{30} \frac{\Gamma(r^+, s^+, \omega^+)}{\phi_{pp}(\omega^+)} dr^+ ds^+}_{C_{31}} \right). \end{aligned} \quad (4.7)$$

Table 2 shows the value of each term in the right hand side of the above equation at the two Re_τ for the same frequencies chosen in figure 9b. For the lower frequency, we observe that the magnitude of the contribution from the cross-correlations between the regions is comparable to the contribution within the regions. However, at high frequency, the contribution within each region dominates over the cross-correlation between the regions. The real part of the cross-correlations is negative at the lower frequency for $Re_\tau = 180$. As discussed in the previous paragraph, this implies that the phase difference of the

Term	$Re_\tau = 180$		$Re_\tau = 400$	
	$\frac{\omega\delta}{u_\tau} = 36.7$	$\omega^+ = 1$	$\frac{\omega\delta}{u_\tau} = 50.2$	$\omega^+ = 1$
C_{11}	1.45	0.87	2.3	0.9
C_{22}	0.67	0.02	3.03	0.04
C_{33}	0.87	0.02	1.08	0.001
$2Re(C_{12})$	-0.76	0.038	-3.65	0.06
$2Re(C_{23})$	-0.44	0.005	-1.83	-0.003
$2Re(C_{31})$	-0.76	0.039	0.09	0.0006

Table 2: Fractional contribution of the inner, overlap and outer region to the wall-pressure fluctuation PSD. For definition of C_{11} , C_{22} , C_{33} , C_{12} , C_{23} and C_{31} , see equation 4.7.

wall-pressure sources in the different regions lie in the range $\pi/2$ to π or $-\pi/2$ to $-\pi$. For the higher Re_τ , except the inner and outer region ($2Re(C_{31})$), the phase difference between all the other regions lie in the same range as the lower Re_τ . Overall, we observe that the cross-correlation between the wall-pressure sources present in the inner, overlap and outer regions are important contributors to the PSD at low frequency but not at high frequency.

Further, this framework can be used to identify the location of the dominant sources that lead to the ω^{-1} behavior of the wall-pressure PSD in the mid frequency range (observed at very high Reynolds numbers). Farabee & Casarella (1991) noted that the ω^{-1} behavior is responsible for the logarithmic dependence of the wall-pressure RMS on Reynolds number (Abe *et al.* 2005; Hu *et al.* 2006; Jimenez & Hoyas 2008).

4.3. Spectral POD of net source CSD

Before we investigate the spectral POD modes of the net source CSD, we first examine the relevance of the modes to wall-pressure fluctuation. We can decompose the wall-pressure fluctuation $p(x, 0, z, t)$ at a typical point (x, z) on the wall by expressing its Fourier transform $\hat{p}(x, 0, z, \omega)$ (equation 3.5) in terms of the spectral POD modes. We have

$$p(x, 0, z, t) = \int_{-\infty}^{+\infty} \hat{p}(x, 0, z, \omega) e^{i\omega t} d\omega, \quad (4.8)$$

$$p(x, 0, z, t) = \int_{-\infty}^{+\infty} \left(\int_{-\delta}^{+\delta} \hat{f}_G(x, y, z, \omega) dy \right) e^{i\omega t} d\omega. \quad (4.9)$$

We use the decomposition in equation 3.18 to express $\hat{f}_G(x, y, z, \omega)$ in terms of the spectral POD modes and obtain

$$p(x, 0, z, t) = \int_{-\infty}^{+\infty} \sum_{j=1}^{\infty} \alpha_j(x, z, \omega) \left(\int_{-\delta}^{+\delta} \Phi_j^*(y, \omega) dy \right) e^{i\omega t} d\omega, \quad (4.10)$$

Rearranging the integral and writing $\Phi_j(y, \omega)$ as $|\Phi_j(y, \omega)|e^{-i\angle\Phi_j(y, \omega)}$, we obtain

$$p(x, 0, z, t) = \int_{-\delta}^{+\delta} \int_{-\infty}^{+\infty} \sum_{j=1}^{\infty} \alpha_j(x, z, \omega) |\Phi_j(y, \omega)| e^{i(-\angle\Phi_j(y, \omega) + \omega t)} d\omega dy. \quad (4.11)$$

The above equation expresses the wall-pressure fluctuation as a contribution from each spectral POD mode. Recall, that the individual contributions are decorrelated, i.e., $\langle \alpha_i(x, z, \omega) \alpha_j^*(x, z, \omega_o) \rangle = \lambda_i(\omega) \delta_{ij} \delta(\omega - \omega_o)$, where δ is the Dirac delta function. Note that since we integrate over all wavenumbers, the contribution of coherent structures of all length scales is included.

The wall-normal phase velocity of the net sources represented by i^{th} spectral POD mode can be quantified as a function of the wall-normal distance using the phase $\angle \Phi_i(y, \omega)$. We define a local wall-normal phase velocity $c_i^+(y^+, \omega^+)$ in viscous units as

$$c_i^+(y^+, \omega^+) = \omega^+ / k_i^+(y^+, \omega^+), \quad (4.12)$$

where the local wavenumber $k_i^+(y^+, \omega^+)$ is defined as $k_i^+(y^+, \omega^+) = \frac{\partial \angle \Phi_i(y^+, \omega^+)}{\partial y^+}$. Note that negative phase velocity indicates an enclosed wave travelling towards the wall and vice versa. Also, this is similar to estimating the instantaneous frequency of a temporal signal using Hilbert transform (Huang & Shen 2014).

We found that, for a wide range of frequencies, setting β (equation 3.16) to 0.1 gives a dominant spectral POD mode (Φ_1) that contributes to all of the wall-pressure PSD (see figure 10). This observation is consistent with the discussion after equation 3.20. Note that the lowest frequency in figure 10 corresponds to the low-frequency peak in the linear PSD. Also, $\omega^+ = 0.35$ is the location of the premultiplied PSD peak. Therefore, the dominant modes at these peak frequencies represent the decorrelated source responsible for the peaks.

Further, the dominant mode represents the active part of the net source Fourier transform ($\hat{f}_G(x, y, z, \omega)$). It is active in the sense that it contributes to the entire PSD. The remaining portion of $\hat{f}_G(x, y, z, \omega)$ is inactive in the sense that it does not contribute to wall-pressure PSD. The suboptimal spectral POD modes comprise this inactive portion. Essentially, the contribution of the suboptimal modes from different wall-normal locations undergo destructive interference resulting in zero net contribution. Since the active and inactive parts of $\hat{f}_G(x, y, z, \omega)$ stem from different modes, they are decorrelated.

Separating the active and inactive parts of $\hat{f}_G(x, y, z, \omega)$ in equation 3.18, we have

$$\begin{aligned} \hat{f}_g(x, y, z, \omega) &= \alpha_1(x, z, \omega) \Phi_1^*(y, \omega) + I(x, y, z, \omega), \\ I(x, y, z, \omega) &= \sum_{j=2}^{\infty} \alpha_j(x, z, \omega) \Phi_j^*(y, \omega), \end{aligned} \quad (4.13)$$

where $\alpha_1(x, z, \omega) \Phi_1^*(y, \omega)$ and $I(x, y, z, \omega)$ are the active and inactive portions of $\hat{f}_G(x, y, z, \omega)$, respectively. Correlating the two, we obtain

$$\begin{aligned} \langle \alpha_1^*(x, z, \omega) \Phi_1(r, \omega) I(x, s, z, \omega_o) \rangle &= \sum_{j=2}^{\infty} \langle \alpha_1^*(x, z, \omega) \alpha_j(x, z, \omega) \rangle \Phi_1(r, \omega) \Phi_j^*(s, \omega_o) \\ &= \sum_{j=2}^{\infty} \lambda_1 \delta_{j1} \Phi_1(r, \omega) \Phi_j^*(s, \omega_o) \text{ (using eqn. 3.18)} \\ &= 0. \end{aligned} \quad (4.14)$$

Therefore, both parts are decorrelated. Note that $I(x, y, z, \omega)$, the inactive part, is orthogonal to the eigenfunction $\Phi_1^*(y, \omega)$ (equation 3.15) in the L^2 inner product. Decreasing β to even smaller values does not affect the mode shape or the eigenvalues for the frequencies in figure 10.

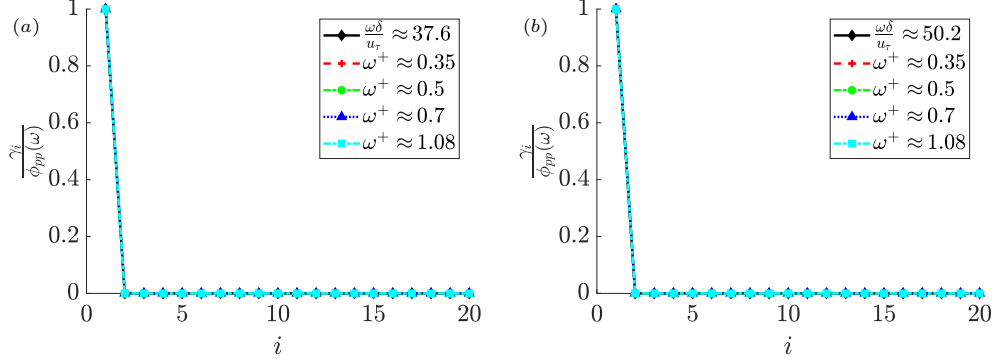


Figure 10: Fractional contribution of the first 20 spectral POD modes computed using the Poisson inner product ($\beta = 0.1$) to the wall-pressure PSD for a) $Re_\tau = 180$ and b) $Re_\tau = 400$ at different frequencies.

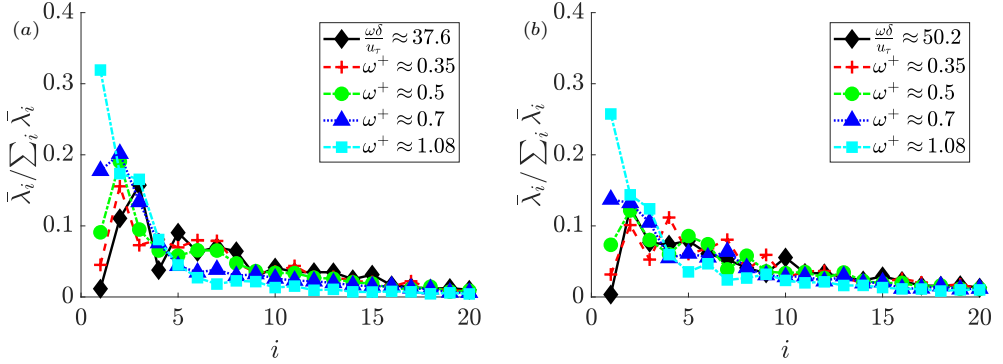


Figure 11: Fractional contribution of the first 20 spectral POD modes computed using the Poisson inner product ($\beta = 0.1$) to the integrated net source PSD for a) $Re_\tau = 180$ and b) $Re_\tau = 400$ at different frequencies.

Since we use a Poisson inner product, the dominant spectral POD mode need not be energetically dominant. In other words, it need not contribute the most to the integrated net source PSD ($\int_{-\delta}^{+\delta} \Gamma(r, r, \omega) dr$). Figure 11 shows this behavior for low frequencies. In the figure, $\bar{\lambda}_j(\omega) = \lambda_j(\omega) |\int_{-\delta}^{+\delta} \Phi_j(y, \omega) dy|^2$ is the contribution of the j^{th} mode to the integrated PSD. We observe that the fractional contribution of the dominant mode increases with frequency. At $\omega^+ = 1$, the dominant spectral POD mode is the energetically dominant mode.

Figure 12 shows the wall-normal variation of the envelope and phase of the dominant mode at the premultiplied spectra peak $\omega^+ = 0.35$ and a few higher frequencies $\omega^+ = 0.5, 0.7$ and 1 . The dominant modes have a similar shape in inner units for both Re_τ . Its envelope (figures 12a and c) represents sources confined near the wall with intensities peaking in the buffer layer. With increasing frequency, the wall-normal location of the peak moves closer to the wall, and the width of the envelope decreases. This behavior of the dominant mode is consistent with that of the wall-pressure fluctuation - net source CSD. The phase (figures 12b and d) of the dominant mode varies between $-\pi/2$ and $\pi/2$.

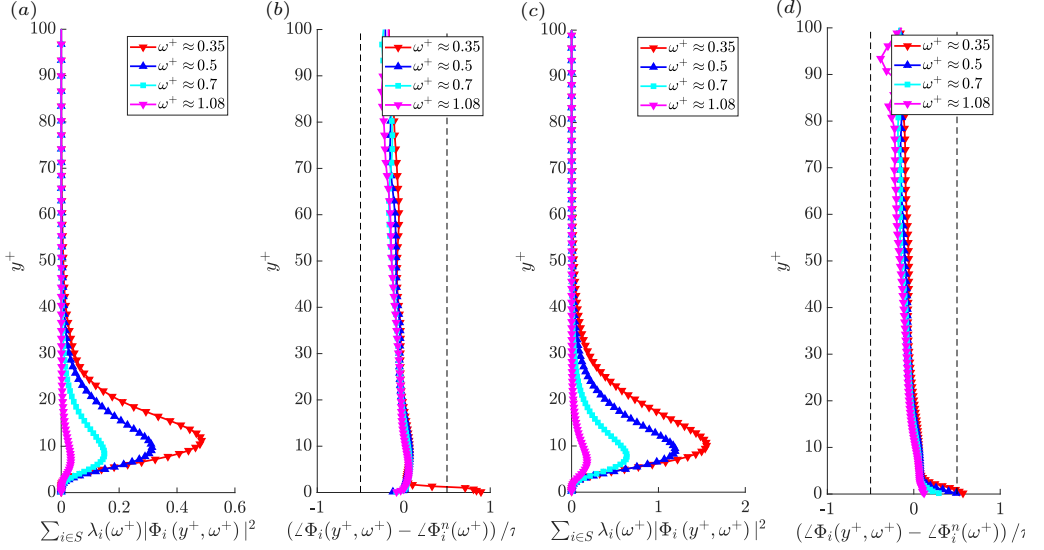


Figure 12: Envelope (figures a, c) and phase (figures b, d) of the dominant spectral POD mode computed using the Poisson inner product ($\beta = 0.1$) for few selected high frequencies. Figures a-b and c-d are for $Re_\tau = 180$ and 400 , respectively. The left and right dashed black solid line in figures b and d indicate $\angle \Phi_i(y^+, \omega^+) - \angle \Phi_i^n(\omega^+)$ equal to $-\pi/2$ and $\pi/2$, respectively.

Therefore, the contributions from different wall-normal locations undergo constructive interference. Further, the phase variation is almost linear with a negative slope, at least around the envelope peak. The negative slope indicates that the envelope encloses a wave traveling towards the wall.

Figures 13a and b show the magnitude and phase, respectively, of the dominant spectral POD mode at the low-frequency linear PSD peak (figure 4). Recall that the frequencies are $\omega\delta/u_\tau = 37.6$ for $Re_\tau = 180$ and 50.2 for $Re_\tau = 400$. The envelope of the dominant mode peaks around $y^+ \approx 15$ for both Re_τ . The phase variation does not show any noticeable slope indicating that the different wall-normal locations are in phase with each other, at least around the envelope peak.

In figure 13c and d, we show the wall-normal contribution of the dominant mode to the wall-pressure PSD. Figure 13c and d are in inner and outer units, respectively. The curves are normalized to obtain unit integral along the y-axis. The contribution peaks at $y^+ \approx 15$ for both Re_τ . Also, figure 13c shows a negative contribution close to the wall for $Re_\tau = 400$ that is not present for $Re_\tau = 180$. We observe that the region $y^+ > 30$ contributes more for the higher Reynolds number, signifying an increase in the outer region contribution. Further, from figure 13d, we observe that the width of this dominant source is around 0.25δ since the y-coordinate is significant for $y < 0.25\delta$. Overall, at the low-frequency PSD peak, the contribution from the dominant mode peaks at $y^+ = 15$, and its width is around 0.25δ .

We create a representative net source field that gives the two-dimensional structure implied by a spectral POD mode. The representative field $\tilde{f}_G(x, y, z, t)$ implied by mode $\Phi_j(y, \omega_o)$ at frequency ω_o is constructed as

$$\tilde{f}_G(x, y, z, t) = \text{Re} \left(\alpha(x, z, \omega_o) e^{-i\angle \Phi_j(y, \omega_o)} |\Phi_j(y, \omega_o)| e^{i\omega_o t} \right), \quad (4.15)$$

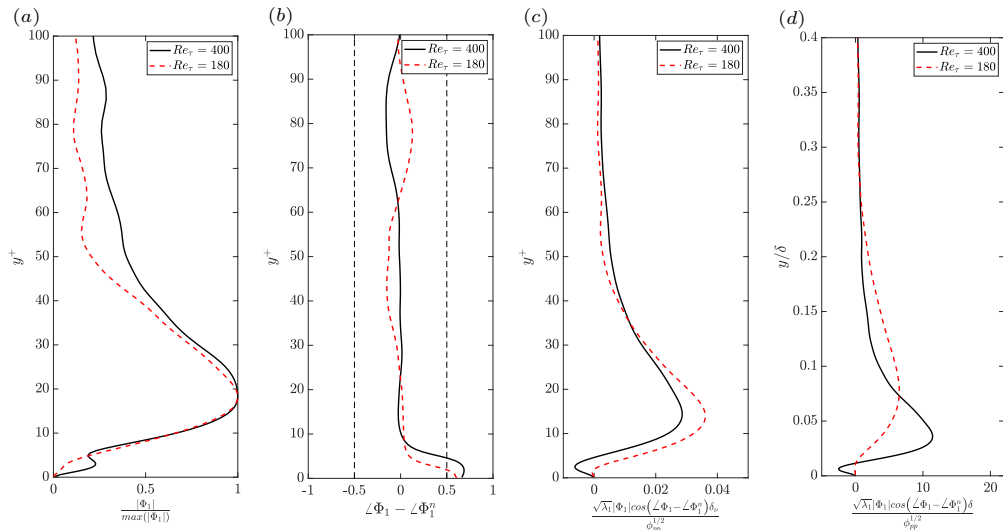


Figure 13: Envelope (figure a) and phase (figure b) of the dominant spectral POD mode compute using the Poisson inner product at the low frequency linear PSD peak. Figures c and d show the normalized wall-normal contribution of the dominant mode to the wall-pressure PSD in inner and outer units, respectively.

where $Re(f)$ is the real part of f . Since $\alpha(x, z, \omega_o)$ is homogenous in x and z , we decompose it using the Fourier transform. Intuitively, we expect the streamwise convective Fourier component $e^{-i\omega_o x/c_o(\omega_o)}$ of $\alpha(x, z, \omega_o)$ to be the most dominant one. Here, $c_o(\omega_o)$ is the convective velocity at frequency ω_o . For simplicity, we assume no spanwise variation of the representative net source. Substituting $\alpha(x, z, \omega_o) = e^{-i\omega_o x/c_o(\omega_o)}$ in the above equation, we obtain the representative field

$$\tilde{f}_G(x, y, z, t) = Re \left(e^{-i\omega_o x/c_o(\omega_o)} e^{-i\angle\Phi_j(y, \omega_o)} |\Phi_j(y, \omega_o)| e^{i\omega_o t} \right). \quad (4.16)$$

To create the representative field at a frequency ω_o , we need three inputs - the mode $\Phi_j(y, \omega_o)$, the convection velocity $c_o(\omega_o)$ and the time t . Figure 14 shows the representative net source field constructed from the dominant spectral POD mode. Figure 14a is at the premultiplied PSD peak frequency and 14b is at the linear PSD peak frequency. We use a convection velocity defined as $c_o(\omega_o)/u_\tau = (\omega_o \delta / u_\tau) / k_p(\omega_o) \delta$, where $k_p(\omega_o)$ is the peak wavenumber coordinate at frequency ω_o in the wavenumber-frequency spectrum of wall-pressure. We choose time t to be 0.

Figures 14a and b show a convecting coherent structure inclined in the downstream direction. Essentially, this is because of the negative slope in the phase of the mode. As the inclined structures convect across a fixed streamwise location x_o^+ , the wall-normal intensity (magnitude of the field that depends on y and x_o) propagates towards the wall as indicated by the negative slope.

Figures 14c and d show the coherent structure represented by the dominant POD mode at the linear PSD peak. These structures are vertical, with almost no inclination in the downstream direction, as indicated by almost no slope in the phase of the mode. Such large scale vertical patterns with streamwise spacing of $\sim 2\delta$ have been previously observed in the instantaneous rapid pressure fields for $Re_\tau \sim 1000$ by Abe *et al.* (2005). They proposed that these patterns are responsible for the low-wavenumber peak in the

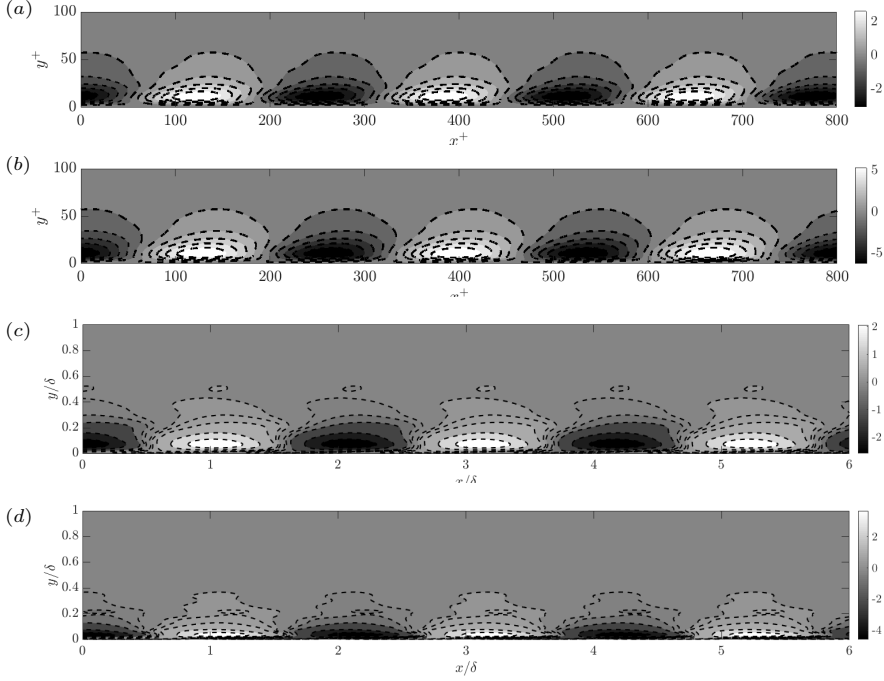


Figure 14: Representative net source \tilde{f}_G at the premultiplied spectra peak (a-b) and the linear spectrum peak (c-d). Figures a and c are for $Re_\tau = 180$, and b and d are for $Re_\tau = 400$. Contours in figures a and b are 10 equally spaced values between the minimum and maximum of \tilde{f}_G . Contours in figures c and d are $[\pm 0.05 \pm 0.1 \pm 0.2 \pm 0.5 \pm 0.8]$ times the maximum value of \tilde{f}_G

wall-pressure spectra. The coherent structures in figures 14c and d further support this case.

Overall, the dominant spectral POD mode represents the active portion of the net source that contributes to the entire wall-pressure PSD. The remaining POD modes that comprise the inactive portion have zero contribution to the PSD. Further, the active and inactive parts are decorrelated. At high frequencies ($\omega^+ \geq 0.35$), the shape of the dominant POD mode is similar in inner units for the two Re_τ . The two-dimensional (2D) coherent structure at the premultiplied PSD peak inclines in the downstream direction. At the low-frequency linear PSD peak, the wall-normal contribution peaks in the buffer layer at $y^+ \approx 15$ with a width of $y/\delta \approx 0.25$. The corresponding 2D structure has a large scale vertical pattern similar to the previous observations of the instantaneous rapid pressure field by Abe *et al.* (2005).

We expect the similarity of the high frequency dominant modes in inner units to continue at even higher Reynolds numbers. At the low wavenumber/frequency wall-pressure linear spectra peak, the outer region ($y^+ > 30$) contributes more for $Re_\tau = 400$ than for $Re_\tau = 180$. This low wavenumber/frequency peak is present in the linear wall-pressure spectra up to $Re_\tau = 5000$ (Panton *et al.* 2017; Abe *et al.* 2005). With increasing Reynolds number, we expect this contribution from the outer region to grow larger. Further, at $Re_\tau \approx 5000$, the low and high wavenumber contributions to the premultiplied wall-pressure spectra show mild separation. We expect the spectral POD modes responsible for the low wavenumber peak to depend on outer units. Further, high

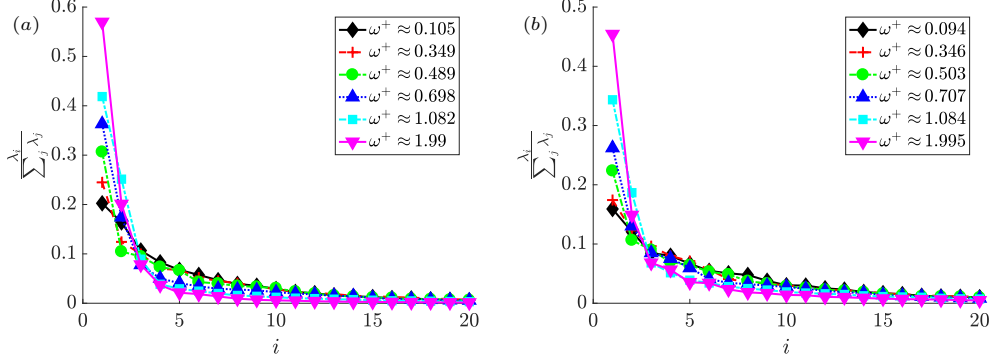


Figure 15: Spectral POD eigenvalues computed using the L^2 inner product for a) $Re_\tau = 180$ and b) $Re_\tau = 400$ at different frequencies.

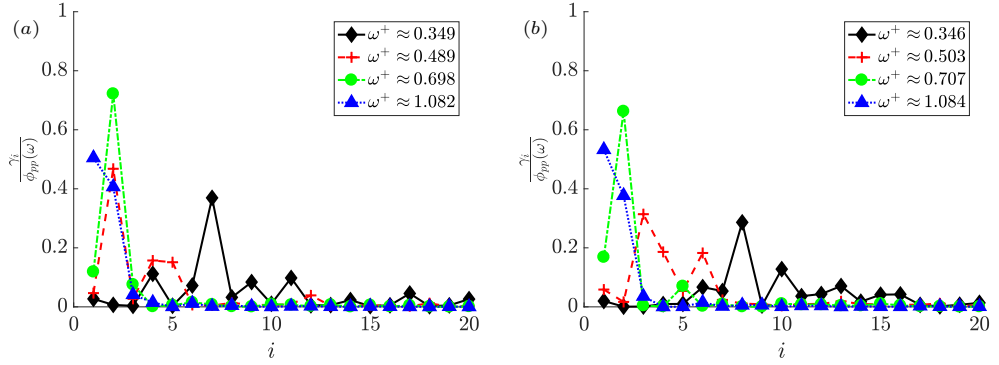


Figure 16: Contribution of the first 20 spectral POD modes computed using the L^2 inner product (normalized by the wall-pressure PSD) to wall-pressure PSD for a) $Re_\tau = 180$ and b) $Re_\tau = 400$ at different frequencies.

Reynolds number effects like amplitude modulation (Tsuji *et al.* 2016) in the wall-pressure sources could be studied using the above spectral POD framework.

4.3.1. Remark on spectral POD with the L^2 inner product

We also performed spectral POD of the net source CSD using the L^2 inner product. Figure 15 shows the obtained eigenvalues for both Re_τ . The eigenvalues give the contribution of each POD mode to the wall-normal integral of the net source PSD. The POD modes obtained with the L^2 inner product, by definition, optimally decompose the integral of the net-source PSD. However, the dominant POD mode might not contribute significantly to the wall-pressure PSD. Clearly, figure 16 shows this behavior for $\omega^+ < 1$.

To investigate this further, we plot the index of the POD mode that contributes the most to the wall-pressure PSD as a function of frequency in figure 17. In the frequency ranges $0.55 < \omega^+ < 1$ and $\omega^+ > 1$, the dominant wall-pressure mode (largest $\gamma_i(\omega)$) is the second and the first spectral POD mode, respectively. At low frequencies $\omega^+ < 0.55$, the dominant wall-pressure mode index is larger than or equal to 3. The dominant spectral POD mode is not the dominant wall-pressure mode because of destructive interference.

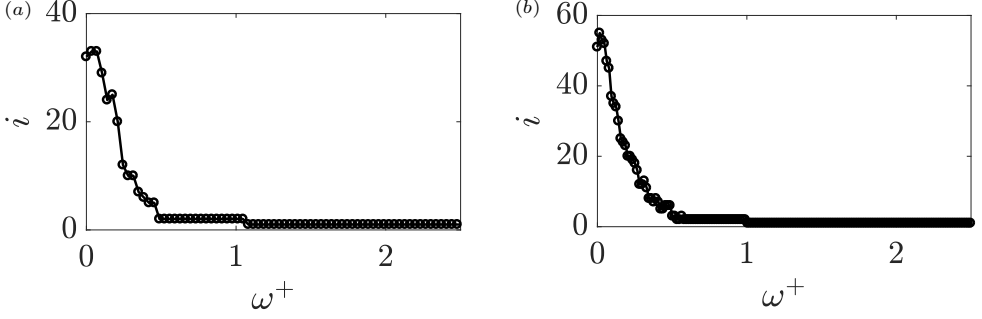


Figure 17: Index of the spectral POD (computed using L^2 inner product) that contributes the most to the wall-pressure PSD for a) $Re_\tau = 180$ and b) $Re_\tau = 400$.

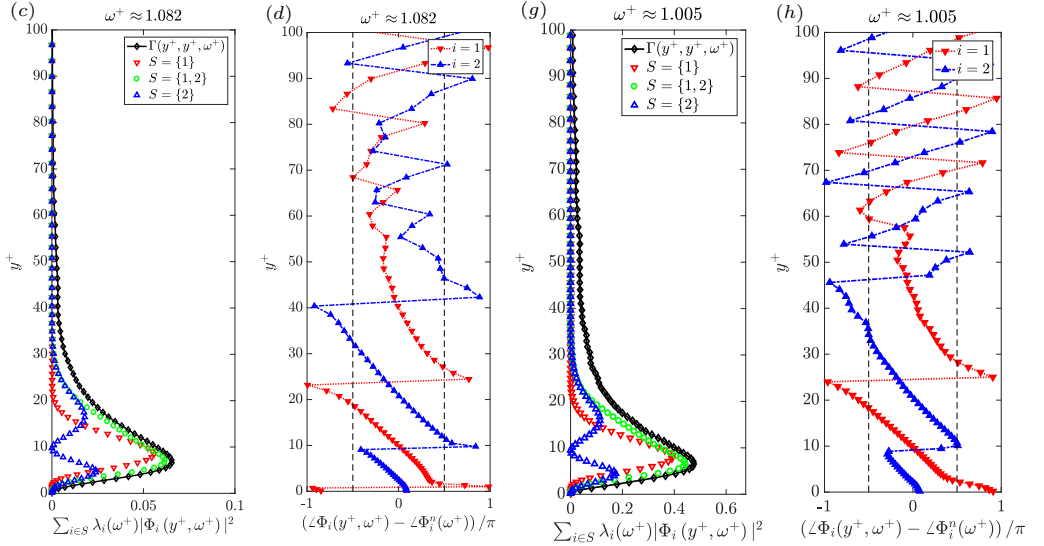


Figure 18: Envelope (figures a, c) and phase (figures b, d) of the two dominant spectral POD modes computed using the L^2 inner product at different frequencies. Figures a-b and c-d are for $Re_\tau = 180$ and 400 , respectively. The left and right dashed black solid line in figure b, d, f and h indicate $\angle \Phi_i(y^+, \omega^+) - \angle \Phi_i^n(\omega^+)$ equal to $-\pi/2$ and $\pi/2$, respectively.

The contributions of the dominant spectral POD mode from different wall-normal regions cancel each other out. For more details, we refer the reader to Appendix D.

The magnitude and phase of the first two dominant spectral POD modes at a high frequency of $\omega^+ \approx 1$ are shown in figure 18. Note that for this frequency, the dominant spectral POD and wall-pressure modes coincide. Clearly, we observe that the dominant modes resemble wavepackets. For both Re_τ , the envelope and phase of the wavepackets have similar shape, which indicates similarity of the dominant modes at high frequencies. The envelope shows that dominant modes correspond to sources in the near wall region ($y^+ < 30$). The first and second dominant mode envelopes have one and two lobes respectively (figures 18a, c, e and g). Since the slope of the phase variation of both

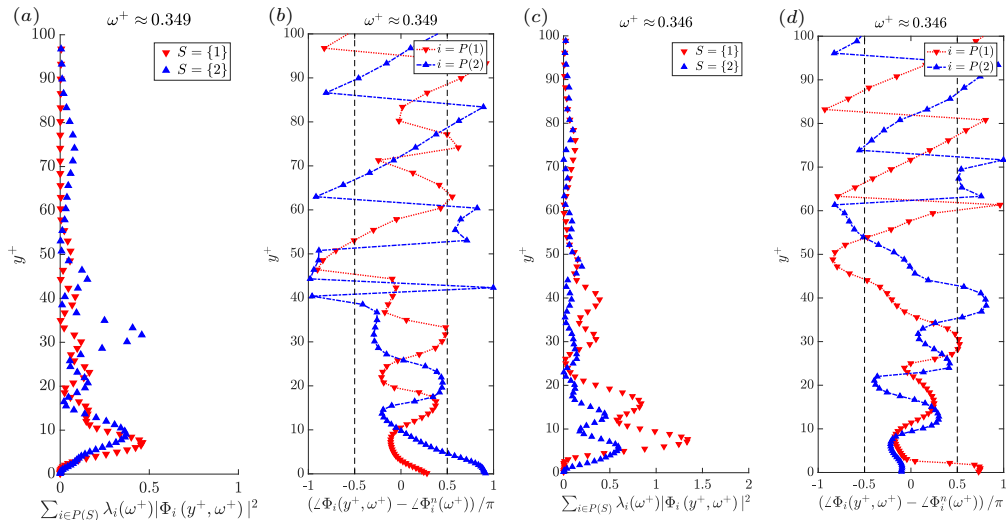


Figure 19: Envelope (figures a, c) and phase (figures b, d) of the two dominant wall-pressure modes computed using the L^2 inner product at $\omega^+ = 0.35$. Figures a-b and c-d are for $Re_\tau = 180$ and 400 , respectively. The left and right dashed black solid line in figures b and d indicate $\angle \Phi_i(y^+, \omega^+) - \angle \Phi_i^n(\omega^+)$ equal to $-\pi/2$ and $\pi/2$, respectively. $P(S)$ is the spectral POD mode index of the S^{th} dominant wall-pressure mode.

modes is negative near the wall (figures 18b, d, f and h), equation 4.12 implies that these modes correspond to sources moving towards the wall.

Next, we investigate the first two dominant wall-pressure modes at $\omega^+ = 0.35$, which together contribute approximately 50% to the wall-pressure PSD in figure 19. Note that the premultiplied spectra peak occurs at this frequency (figure 1b). The magnitude and phase variation shows that these modes do not resemble a near-wall wavepacket. The envelope is not localized and the phase variation shows no sign of linear variation. Not much can be said of the pattern of these low frequency wall-pressure sources, except that the contributions from different wall-normal regions undergo constructive interference. This is because the phase of the mode varies mostly between the two dashed lines. Further, several suboptimal spectral POD modes each contribute a small fraction the wall-pressure PSD at this frequency (figure 16). Thus, the individual dominant wall-pressure mode obtained using the L^2 inner product does not give us much information of the wall-pressure sources. However, the mode obtained using the Poisson inner product with $\beta = 0.1$ (figure 12) gives useful information of the wall-pressure source.

Therefore, spectral POD using the Poisson inner product performs better than the L^2 inner product in isolating dominant wall-pressure sources for both low and high frequencies. This is because the Poisson inner product decomposes the integral $\iint_{-\delta}^{+\delta} \frac{G(s, r, \frac{\beta}{1-\beta}, 0)}{1-\beta} \Gamma(r, s, \omega) dr ds$ as sum of eigenvalues. For small enough β , this integral is a good proxy for wall-pressure PSD. On the other hand, the L^2 inner product decomposes the integrated net source PSD ($\int_{-\delta}^{+\delta} \Gamma(r, s, \omega) dr$) instead which is not a good proxy for wall-pressure PSD.

5. Summary

We present a novel framework to analyze the sources of wall-pressure fluctuation in turbulent channel flow. A net source function $f_G(y, t)$ is defined whose integral in the wall-normal direction gives the wall-pressure fluctuation, i.e., $p(t) = \int_{-\delta}^{+\delta} f_G(y, t) dy$. The spectral properties of the defined net source function are studied by computing its CSD using the generated DNS dataset at $Re_\tau = 180$ and 400. The wall-pressure fluctuation - net source CSD shows a premultiplied peak at $\omega^+ = 0.35$ for both Re_τ . The wall-normal location corresponding to the peak is $y^+ = 16.5$ and 18.4 for $Re_\tau = 180$ and 400, respectively. Therefore, the peak in the premultiplied wall-pressure PSD at $\omega^+ = 0.35$ is due to the correlation with the sources in buffer layer. The wall-pressure fluctuation - net source CSD has a log-normal behavior in y^+ for $\omega^+ > 0.35$. The location of the dominant wall-parallel plane obtained from the mean of the log-normal profile varies exponentially with frequency. The wall-normal width of the dominant region obtained from the standard deviation of the log-normal profile is approximately proportional to the location of the dominant plane. At low frequencies, a dominant inner and overlap/outer region interaction is observed at both Re_τ .

We obtain the decorrelated net source patterns by performing spectral POD of the net source CSD using an inner product that has a symmetric positive definite kernel. The net source can be decomposed into active and inactive parts. The dominant spectral POD mode identified with this new inner product is active in the sense that it contributes to the entire wall-pressure PSD. The remaining portion of the net source constituted by the suboptimal POD modes is inactive in the sense that it does not contribute to wall-pressure PSD. Further, the active and inactive portions of the net source are decorrelated.

The dominant mode at the premultiplied PSD peak ($\omega^+ \approx 0.35$) has a similar shape in inner units for both Re_τ . It represents structures inclined in the downstream direction. At the low frequency linear PSD peak, the wall-normal contribution peaks at $y^+ \approx 15$ and has a width of $y/\delta \approx 0.25$. The corresponding two-dimensional structure has a large scale vertical pattern similar to the observations of Abe *et al.* (2005) in the instantaneous fields of rapid pressure.

The analysis framework presented in this paper can be used to quantitatively understand the contribution of large scale coherent motions in the outer region at very high Reynolds numbers. Such contributions are believed to be the reason for the increasing low wavenumber contribution to wall-pressure RMS (Panton *et al.* 2017). The analysis has implications on wall modelled large eddy simulations (LES). The wall-pressure fluctuation net source CSD shows that sources correlated with the buffer layer are essential contributors to the premultiplied power spectra peak at $\omega^+ = 0.35$. However, in wall modelled LES where the first point is in the logarithmic layer, one would not resolve the net source terms that lie in the buffer region. Hence, wall-modeled LES would fail to accurately predict the wall-pressure spectra at high frequencies. These conclusions are consistent with Bradshaw (1967) who noted the importance of buffer layer eddies to the higher frequencies in the wall-pressure spectra, and are consistent with Park & Moin (2016) who attribute the errors in the high frequency slope of wall-pressure spectrum to the lack of resolution of the buffer layer eddies in their wall modeled LES. Also, high Reynolds number effects like amplitude modulation of wall-pressure (Tsuji *et al.* 2016) can be studied using the above framework. The framework can also be used to quantitatively investigate the location of the sources that lead to ω^{-1} decay in the wall-pressure PSD at high Reynolds numbers.

Acknowledgements

This work is supported by the United States Office of Naval Research (ONR) under grant N00014-17-1-2939 with Dr. Ki-Han Kim as the technical monitor. The computations were made possible through computing resources provided by the US Army Engineer Research and Development Center (ERDC) in Vicksburg, Mississippi on the Cray X6, Copper and Onyx of the High Performance Computing Modernization Program.

Appendix A. Implementation details

The theory presented in section 3.1 considers infinite domains in spanwise and streamwise directions. Here, we present the implementation for finite periodic domains instead. The integrals over the wavenumbers are replaced by a summation over the discrete wavenumbers that can be represented in the periodic domain. The wavenumber spacing is determined by the length of the domain in each direction.

Let N_t be the number of timesteps in each chunk used to compute the Fast Fourier Transform (FFT), N_T be the total number of timesteps for which the data is acquired, n_c be the number of chunks used for temporal averaging the computed spectra, T_c be the span of each chunk and p_{ovp} be the percentage overlap between subsequent chunks.

The angular wavenumbers and frequencies are defined as

$$k_l^x = \frac{2\pi l}{L_x}; k_m^z = \frac{2\pi m}{L_z}; \omega_n = \frac{2\pi n}{T_c}; \quad (\text{A } 1)$$

$$l = -N_x/2, \dots, N_x/2 - 1; m = -N_z/2, \dots, N_z/2 - 1; n = -N_t/2, \dots, N_t/2 - 1.$$

We store the source terms of the pressure Poisson equation in hard disk from the finite volume solver. The domain in the finite volume solver is split into multiple processors and each processor writes one file per run containing the time history of the source terms of the control volumes in its partition. A total of $\approx 8TB$ and $\approx 30TB$ was required to store the source terms of the pressure Poisson equation for the $Re_\tau = 180$ and $Re_\tau = 400$ cases respectively.

The portion of the time series that corresponds to the current chunk being processed is first converted to stationary frame of reference and then written to a scratch space as wall-parallel slices. Let \bar{f} denote the four-dimensional source term array in the moving frame of reference corresponding to the current chunk. i.e.,

$$\bar{f} = \{\bar{f}_{i,j,k,l} \mid i = 0, \dots, N_x - 1, j = 0, \dots, N_y - 1, k = 0, \dots, N_z - 1, l = 0, \dots, N_t - 1\},$$

$$\bar{f}_{i,j,k,l} = D_{x_n} u_m D_{x_m} u_n|_{x_i, y_j, z_k, t_l}, \quad (\text{A } 2)$$

where $D_{x_n} u_m D_{x_m} u_n$ is the discrete approximation to right hand side of the pressure Poisson equation. The data is converted to stationary frame of reference using Fourier interpolation and stored in the source term array f as

$$f = \{f_{i,j,k,l} \mid i = 1, \dots, N_x, j = 1, \dots, N_y, k = 1, \dots, N_z, l = 1, \dots, N_t\},$$

$$f_{i,j,k,l} = \sum_{m=-N_x/2}^{N_x/2-1} \tilde{f}_{m,j,k,l} e^{-ik_m^x U_c t_l} e^{ik_m^x x_i}, \quad (\text{A } 3)$$

$$\tilde{f}_{m,j,k,l} = \frac{1}{N_x} \sum_{i=0}^{N_x-1} \bar{f}_{i,j,k,l} e^{-ik_m^x x_i}.$$

Multiple processors are used to transfer the data from the Cartesian decomposition

of the solver to a wall-parallel decomposition of the computational domain. The wall-parallel decomposition facilitates the computation of the wavenumber frequency cross spectra of the source terms. In order to obtain the fluctuation, the temporal mean of the array f at each spatial point is subtracted to ensure that it has zero mean. i.e.,

$$\begin{aligned} f_{i,j,k,l} &= f_{i,j,k,l} - \langle f \rangle_{i,j,k}, \\ \langle f \rangle_{i,j,k} &= \frac{1}{N_t} \sum_{l=0}^{N_t-1} f_{i,j,k,l}. \end{aligned} \quad (\text{A } 4)$$

Each of the wall-parallel slices stoblack in the scratch space is then Fourier transformed in streamwise, spanwise directions and in time. Let \hat{f} denote the Fourier transformed f . Then,

$$\begin{aligned} \hat{f} &= \{ \hat{f}_{i,j,k,l} \mid i = -N_x/2, \dots, N_x/2 - 1, j = 0, \dots, N_y - 1, \\ &\quad k = -N_z/2, \dots, N_z/2 - 1, l = -N_t/2, \dots, N_t/2 - 1 \}, \\ \hat{f}_{i,j,k,l} &= \frac{1}{N_x N_z N_t} \sum_{m,n,p=1}^{N_x-1, N_z-1, N_t-1} f_{m,j,n,p} w_p e^{-i(k_i^x x_m + k_k^z z_n + \omega_l t_p)}, \end{aligned} \quad (\text{A } 5)$$

where $w_p = \sin^2(\pi p/N_t)$ is the Hanning Window function multiplied with the time series in order to avoid spectral leakage. The wall-parallel slice data is over written by its three-dimensional Fourier transform. The processors are split in the wall-normal and time directions to carry out the task in parallel and we use the parallel-FFTW (Frigo & Johnson 2005) library to carry out the Fourier transform.

As discussed in the previous section, the memory requirement to store the five-dimensional function $\phi_{ff}(r, s, k_1, k_3, \omega)$ is too large. We store and append the net source cross spectral density sum array Γ^s (defined below) instead. The possible $\{r_i, s_j\}_{i,j=1}^{N_y}$ pairs are split among multiple processors. For each (r_i, s_j) pair, we read the arrays $\hat{f}_{:,i,:}$ and $\hat{f}_{:,j,:}$ from the scratch space and update the sum $\Gamma_{i,j,:}^s$ as

$$\begin{aligned} \Gamma^s &= \{ \Gamma_{i,j,k}^s \mid i = 1, \dots, N_y, j = 1, \dots, N_y, k = -N_t/2, \dots, N_t/2 - 1 \}, \\ \Gamma_{i,j,k}^s &= \Gamma_{i,j,k}^s + \frac{8}{3} \frac{T}{2\pi} \frac{L_1}{2\pi} \frac{L_3}{2\pi} \sum_{l=-N_x/2}^{N_x/2-1} \sum_{m=-N_z/2}^{N_z/2-1} \hat{f}_{l,i,m,k}^* \hat{f}_{l,j,m,k} G_{i,l,m}^* G_{j,l,m} \frac{2\pi}{L_1} \frac{2\pi}{L_3}, \end{aligned} \quad (\text{A } 6)$$

$$G_{i,l,m} = G(0, y_i, k_l, k_m).$$

The factor $8/3$ in the above equation accounts for the blackuction in the spectral magnitude due to windowing (Bendat & Piersol 2011). The update to $\Gamma_{i,j,:}^s$ given in the above equation A 6 is carried out in chunks along the frequency dimension due to limited memory available in a cluster node. The net source cross spectral density Γ array is then defined by dividing the Γ^s array by the number of chunks n_c , i.e.

$$\Gamma = \{ \Gamma_{i,j,k} \mid \Gamma_{i,j,k} = \Gamma_{i,j,k}^s / n_c, i = 1, \dots, N_y, j = 1, \dots, N_y, k = -N_t/2, \dots, N_t/2 - 1 \}. \quad (\text{A } 7)$$

We store and append only half of the entire Γ^s array since $\Gamma_{j,i,k} = \Gamma_{i,j,k}^*$. We use 50% overlap between the chunks to increase statistical convergence. As new chunk data become available, the net source cross spectral density Γ^s is updated.

Note that the Green's function had to be evaluated in quadruple precision for $Re_\tau = 400$ because for some wavenumbers, both the numerator and denominator were so large that it could not be stoblack in double precision. However, when divided, the resulting number could be stoblack in double precision. The above post-processing methodology is

parallel, aware of the limited memory available in a supercomputer cluster node and can be used to analyze even larger channel flow datasets obtained for higher friction Reynolds numbers.

To obtain the spectral POD modes, we first obtain the eigenvalues $\{\lambda_{i,l}\}_{i=1}^{N_y}$ and the eigenvectors $\{\bar{\varphi}_{i,l}\}_{i=1}^{N_y}$ of the problem

$$\begin{aligned} A_l \bar{\varphi}_{i,l} &= \lambda_{i,l} W \bar{\varphi}_{i,l}; \quad i = 1, \dots, N_y, \quad l = -N_t/2, \dots, N_t/2 - 1, \\ A_l &= \{A_l \in \mathbb{C}^{N_y \times N_y} \mid \{A_l\}_{m,n} = \Delta y_m \Gamma_{m,n,l} \Delta y_n\}, \end{aligned} \quad (\text{A } 8)$$

where the matrix W is the finite volume discretization of the operator $\left(- (1 - \alpha) \frac{\partial^2}{\partial y^2} + \alpha\right)$. The spectral POD eigenvalues are $\{\lambda_{i,l}\}_{i=1}^{N_y}$ and eigenvectors are $\{\varphi_{i,l}\}_{i=1}^{N_y}$, where $\{\varphi_{i,l}\}_{i=1}^{N_y}$ is related to $\{\bar{\varphi}_{i,l}\}_{i=1}^{N_y}$ as

$$\begin{aligned} \varphi_{i,l} &= D^{-1} W \bar{\varphi}_{i,l}; \quad i = 1, \dots, N_y, \quad l = -N_t/2, \dots, N_t/2 - 1, \\ D &= \{D \in \mathbb{C}^{N_y \times N_y} \mid \{D\}_{m,n} = \Delta y_m \delta_{mn}\} \end{aligned} \quad (\text{A } 9)$$

Appendix B. Orthogonality of the linear transformation C

We prove the orthogonality relation given by equation 3.22. Writing the Fourier transform of the net source function as a linear combination of the set of modes $\{\hat{\Phi}_i(y, \omega)\}_{i=1}^{\infty}$ and $\{\tilde{\Phi}_i(y, \omega)\}_{i=1}^{\infty}$, we have,

$$\hat{f}_G(x, y, z, \omega) = \sum_j \hat{\alpha}_j(x, z, \omega) \hat{\Phi}_j^*(y, \omega) = \sum_j \tilde{\alpha}_j(x, z, \omega) \tilde{\Phi}_j^*(y, \omega), \quad (\text{B } 1)$$

where $\hat{\alpha}(\omega)$ and $\tilde{\alpha}(\omega_o)$ are the coefficients of the linear combination. For brevity, we drop the dependence of $\hat{\alpha}$ and $\tilde{\alpha}$ on x and z . Using equation 3.21 in B 1 and equating the coefficients of $\{\tilde{\Phi}_j^*\}_{j=1}^{\infty}$, we have

$$\sum_j \hat{\alpha}_j(\omega) C_{jk}(\omega) = \tilde{\alpha}_k(\omega) \quad (\text{B } 2)$$

Correlating the coefficients, we have

$$\langle \tilde{\alpha}_k(\omega) \tilde{\alpha}_l^*(\omega_o) \rangle = \sum_j \sum_m \langle \hat{\alpha}_j(\omega) \hat{\alpha}_m^*(\omega_o) \rangle C_{jk}(\omega) C_{ml}^*(\omega_o). \quad (\text{B } 3)$$

Since the coefficients are decorrelated, we obtain

$$\tilde{\lambda}_k(\omega) \delta_{kl} \delta(\omega - \omega_o) = \sum_j \sum_m \hat{\lambda}_j \delta_{jm} \delta(\omega - \omega_o) C_{jk}(\omega) C_{ml}^*(\omega_o). \quad (\text{B } 4)$$

Integrating in ω_o and expression the above relation in matrix form, we have

$$\tilde{\Lambda}(\omega) = C^H(\omega) \hat{\Lambda}(\omega) C(\omega). \quad (\text{B } 5)$$

where $\tilde{\Lambda}(\omega)$ and $\hat{\Lambda}(\omega)$ are the diagonal matrices of the eigenvalues. Since the eigenvalues are non-negative, we decompose $\hat{\Lambda}(\omega)$ as $\hat{\Lambda}^{1/2}(\omega) \hat{\Lambda}^{1/2}(\omega)$, respectively, where $\hat{\Lambda}^{1/2}(\omega)$ is a diagonal matrix constructed using the set of values $\{\sqrt{\lambda_i(\omega)}\}_{i=1}^{\infty}$, and obtain the requiblack result

$$\left(\hat{\Lambda}^{1/2}(\omega) C(\omega) \right)^H \hat{\Lambda}^{1/2}(\omega) C(\omega) = \tilde{\Lambda}(\omega). \quad (\text{B } 6)$$

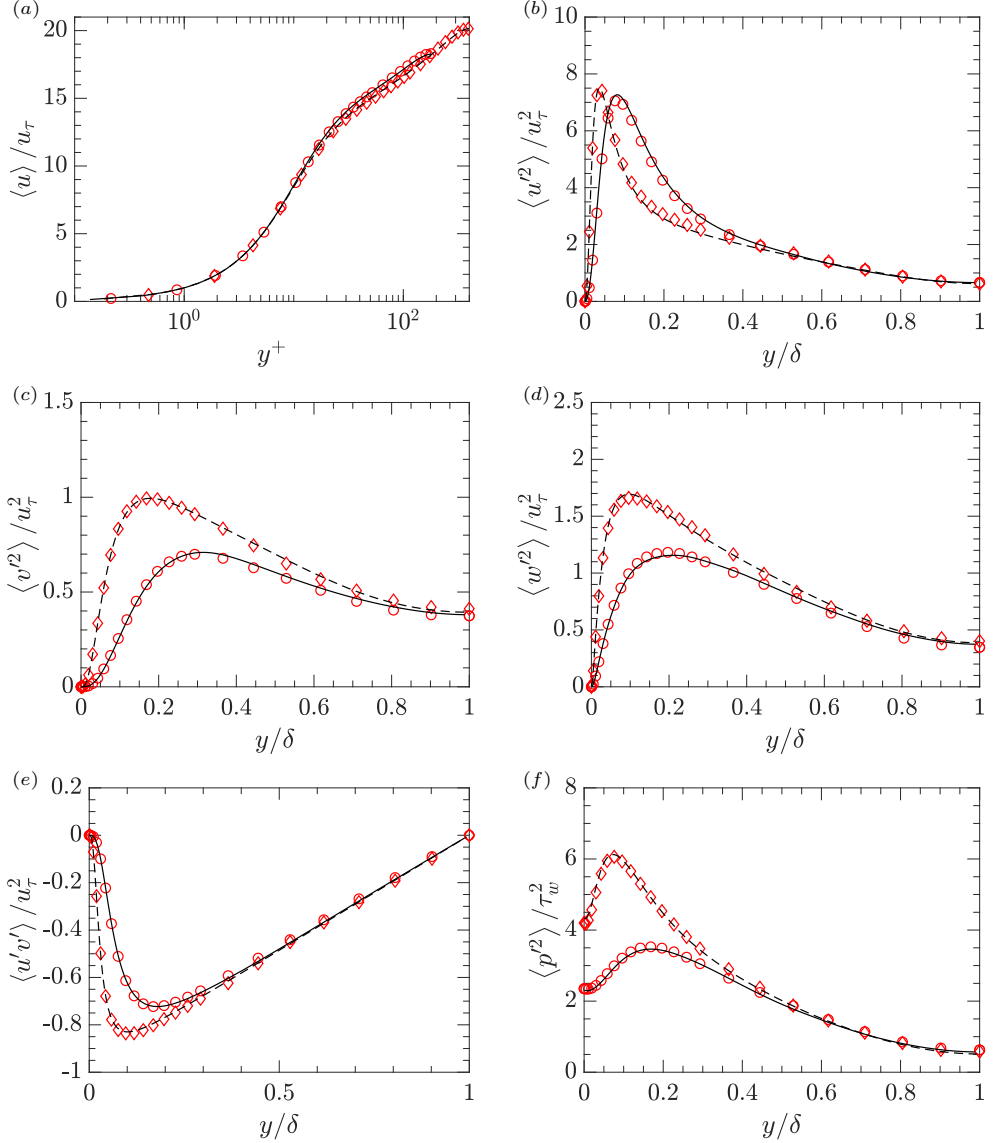


Figure 20: Velocity field and pressure fluctuation statistics. Solid and dashed lines denote the current DNS result at $Re_\tau = 180$ and 400 , respectively. Circle and diamond symbols denote DNS data at $Re_\tau = 182$ and 392 from Moser *et al.* (1999). Figure a compares mean streamwise velocity, figures b, c, d compare mean-squared streamwise, wall-normal and spanwise velocity fluctuation, respectively, and figures e and f compare mean tangential Reynolds stress and mean-squared pressure fluctuation, respectively.

Appendix C. DNS validation

We compare the mean, intensities and spectra from the current DNS to the previous reference DNS. We sample the velocity and pressure field every 50 timesteps to compute the statistics presented in this section.

Figure 20 shows the comparison of velocity field and pressure fluctuation statistics

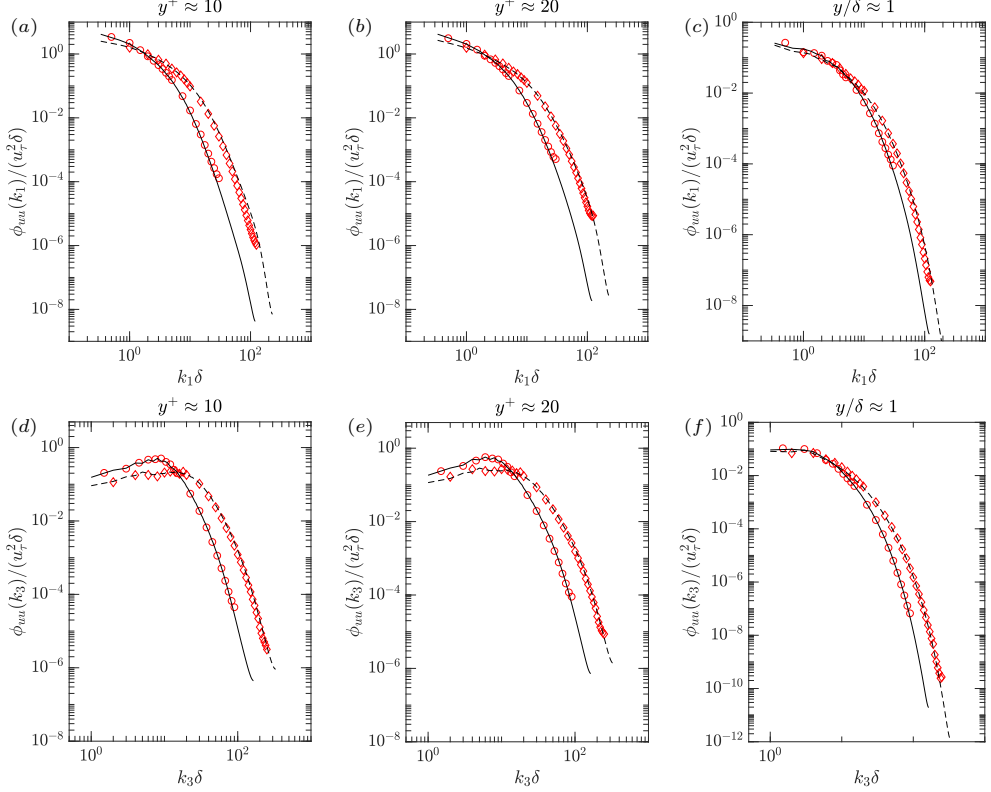


Figure 21: Streamwise velocity fluctuation spectra. Figures a-c and d-f are streamwise and spanwise wavenumber spectra, respectively at different wall-normal locations. Solid and dashed lines denote the current DNS result at $Re_\tau = 180$ and 400 , respectively. Circle and diamond symbols denote DNS data at $Re_\tau = 182$ and 392 from Moser *et al.* (1999).

to the previous DNS of Moser *et al.* (1999) performed at $Re_\tau = 182$ and 392 . Figure 20a compares mean streamwise velocity. Figures 20b, c and d compare mean-squared streamwise, wall-normal and spanwise velocity fluctuation, respectively. Figures 20e and f compare mean tangential Reynolds stress and mean-squared pressure fluctuation, respectively. We observe good agreement in the computed quantities.

Figure 21 compares both streamwise and spanwise wavenumber spectra of the streamwise velocity fluctuations to the previous DNS of Moser *et al.* (1999) at different wall-normal locations. We compare the spectra at $y^+ \approx 10$ (near the buffer layer peak in the intensity), $y^+ \approx 20$ and $y/\delta \approx 1$ (channel centerline). The current spectra agree well both near the wall and at the channel center for the two Re_τ . Therefore, the DNS is well-resolved.

In figure 22, we compare the streamwise and spanwise wavenumber spectra of the pressure fluctuations to Moser *et al.* (1999) at $y^+ \approx 5$ (near the wall), $y^+ \approx 30$ (at the peak intensity location) and $y/\delta \approx 1$ (channel centerline). The spectra show good agreement. Also, we do not observe the spurious pile up of the spectrum levels at very high wavenumbers seen in the results of Moser *et al.* (1999).

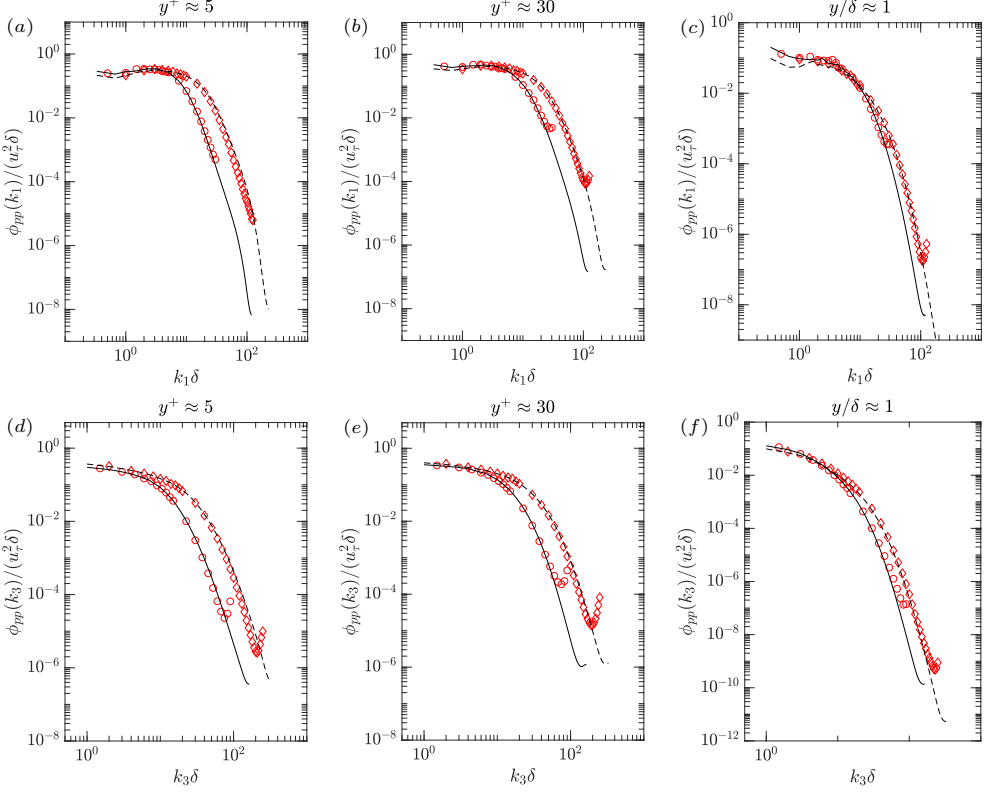


Figure 22: Pressure fluctuation spectra. Figures a-c and d-f are streamwise and spanwise wavenumber spectra, respectively at different wall-normal locations. Solid and dashed lines denote the current DNS result at $Re_\tau = 180$ and 400 , respectively. Circle and diamond symbols denote DNS data at $Re_\tau = 182$ and 392 from Moser *et al.* (1999).

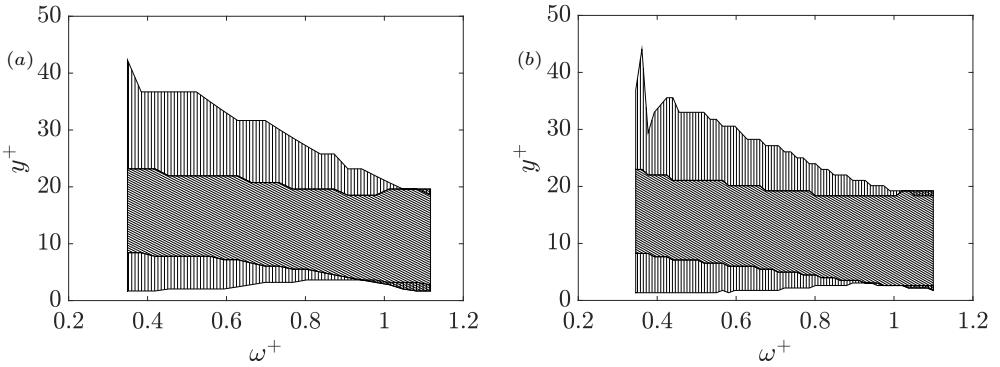


Figure 23: Comparison of destructively interfering regions of the dominant spectral POD mode computed using the L^2 inner product as a function of frequency for a) $Re_\tau = 180$ and b) $Re_\tau = 400$. In the cross and vertically hatched regions, $|\angle \Phi_i(y^+, \omega^+) - \angle \Phi_i^n(\omega^+)| < \pi/2$ and $\pi/2 < |\angle \Phi_i(y^+, \omega^+) - \angle \Phi_i^n(\omega^+)| < \pi$, respectively.

Appendix D. Destructive interference of dominant L^2 inner product mode contribution to wall-pressure PSD

We investigate the frequency dependence of the destructive interference of the obtained dominant spectral POD mode (computed using the L^2 inner product) in figure 23. The envelope and the phase of the wavepacket are used to identify destructively interfering regions. In the figure, the vertical and cross-hatched regions of the mode interfere destructively. In the cross-hatched and vertically hatched regions, the phase satisfies $|\angle\Phi_i(y, \omega) - \angle\Phi_i^n(\omega)| < \pi/2$ and $\pi/2 < |\angle\Phi_i(y, \omega) - \angle\Phi_i^n(\omega)| < \pi$, respectively. With increase in frequency, the ratio of the cross and vertically hatched region increases. Therefore, the destructive interference in the contribution from the dominant spectral POD mode to wall-pressure PSD decreases. Hence, the dominant spectral POD mode becomes the dominant wall-pressure mode for $\omega^+ \geq 1$ (figure 17). For small frequencies, the dominant spectral POD mode does not resemble a wall-normal wavepacket. Therefore, we would not obtain a continuously (continuous in frequency) varying interface between the destructively interfering region. Therefore, we do not include the frequencies below $\omega^+ = 0.35$.

REFERENCES

- ABE, HIROYUKI, MATSUO, YUICHI & KAWAMURA, HIROSHI 2005 A dns study of reynolds-number dependence on pressure fluctuations in a turbulent channel flow. In *Fourth International Symposium on Turbulence and Shear Flow Phenomena*. Begel House Inc.
- BENDAT, J. S. & PIERSON, A. G. 2011 *Random data: analysis and measurement procedures*. John Wiley & Sons.
- BERNARDINI, M., PIROZZOLI, S., QUADRIO, M. & ORLANDI, P. 2013 Turbulent channel flow simulations in convecting reference frames. *J. Comp. Phys.* **232**, 1–6.
- BLAKE, W. K. 1970 Turbulent boundary-layer wall-pressure fluctuations on smooth and rough walls. *J. Fluid Mech.* **44**, 637–660.
- BLAKE, W. K. 2017 *Mechanics of Flow-Induced Sound and Vibration, Volume 1 and 2*. Academic Press.
- BRADSHAW, P 1967 inactivemotion and pressure fluctuations in turbulent boundary layers. *Journal of Fluid Mechanics* **30** (2), 241–258.
- BULL, M. K. 1996 Wall-pressure fluctuations beneath turbulent boundary layers: some reflections on forty years of research. *J. Sound Vib.* **190**, 299–315.
- CHANG III, P. A., PIOMELLI, U. & BLAKE, W. K. 1999 Relationship between wall pressure and velocity-field sources. *Phys. of Fluids* **11**, 3434–3448.
- CHOI, H. & MOIN, P. 1990 On the space-time characteristics of wall-pressure fluctuations. *Phys. Fluids* **2**, 1450–1460.
- CORCOS, G. M. 1964 The structure of the turbulent pressure field in boundary-layer flows. *J. Fluid Mech.* **18**, 353–378.
- DE GRAAFF, D. B. & EATON, J. K. 2000 Reynolds-number scaling of the flat-plate turbulent boundary layer. *J. Fluid Mech.* **422**, 319–346.
- DEL ÁLAMO, J. C. & JIMÉNEZ, J. 2003 Spectra of the very large anisotropic scales in turbulent channels. *Phys. Fluids* **15**, L41–L44.
- FARABEE, T. M. & CASARELLA, M. J. 1991 Spectral features of wall pressure fluctuations beneath turbulent boundary layers. *Phys. Fluids* **3**, 2410–2420.
- FRIGO, M. & JOHNSON, S. G. 2005 The design and implementation of FFTW3. *Proc. IEEE* **93**, 216–231.
- GEROLYMOS, GA, SÉNÉCHAL, D & VALLET, I 2013 Wall effects on pressure fluctuations in turbulent channel flow. *Journal of Fluid Mechanics* **720**, 15–65.
- GRAVANTE, S. P., NAGUIB, A. M., WARK, C. E. & NAGIB, H. M. 1998 Characterization of the pressure fluctuations under a fully developed turbulent boundary layer. *AIAA journal* **36**, 1808–1816.

- HOYAS, SERGIO & JIMÉNEZ, JAVIER 2006 Scaling of the velocity fluctuations in turbulent channels up to $Re_\tau = 2003$. *Physics of fluids* **18** (1), 011702.
- HU, Z., MORFEY, C. L. & SANDHAM, N. D. 2006 Wall pressure and shear stress spectra from direct numerical simulations of channel flow. *AIAA Journal* **44**, 1541–1549.
- HUANG, N. E. & SHEN, S. P. 2014 *Hilbert-Huang transform and its applications*. World Scientific.
- JIMENEZ, JAVIER & HOYAS, SERGIO 2008 Turbulent fluctuations above the buffer layer of wall-bounded flows. *Journal of Fluid Mechanics* **611**, 215–236.
- KIM, J. 1989 On the structure of pressure fluctuations in simulated turbulent channel flow. *J. Fluid Mech.* **205**, 421–451.
- KIM, JOHN & HUSSAIN, FAZLE 1993 Propagation velocity of perturbations in turbulent channel flow. *Physics of Fluids A: Fluid Dynamics* **5** (3), 695–706.
- KIM, J., MOIN, P. & MOSER, R. 1987 Turbulence statistics in fully developed channel flow at low Reynolds number. *J. Fluid Mech.* **177**, 133–166.
- KLEWICKI, J. C., PRIYADARSHANA, P. J. A. & METZGER, M. M. 2008 Statistical structure of the fluctuating wall pressure and its in-plane gradients at high Reynolds number. *J. Fluid Mech.* **609**, 195–220.
- LUMLEY, J. L. 2007 *Stochastic tools in turbulence*. Courier Corporation.
- MAHESH, K., CONSTANTINESCU, G. & MOIN, P. 2004 A numerical method for large-eddy simulation in complex geometries. *J. Comp. Phys.* **197**, 215–240.
- MORRISON, J. F. 2007 The interaction between inner and outer regions of turbulent wall-bounded flow. *Phil. Trans. R. Soc. Lond.* **365**, 683–698.
- MOSER, ROBERT D, KIM, JOHN & MANSOUR, NAGI N 1999 Direct numerical simulation of turbulent channel flow up to $Re_\tau = 590$. *Physics of fluids* **11** (4), 943–945.
- PANTON, R. L., LEE, M. & MOSER, R. D. 2017 Correlation of pressure fluctuations in turbulent wall layers. *Phys. Rev. Fluids* **2**, 094604.
- PARK, G. I. & MOIN, P. 2016 Space-time characteristics of wall-pressure and wall shear-stress fluctuations in wall-modeled large eddy simulation. *Phys. Rev. Fluids* **1**, 024404.
- POPE, STEPHEN B 2001 *Turbulent flows*. Cambridge University Press.
- SCHMIDT, O. T., TOWNE, A., RIGAS, G., COLONIUS, T. & BRÈS, G. A. 2018 Spectral analysis of jet turbulence. *J. Fluid Mech.* **855**, 953–982.
- SILLERO, J. A., JIMÉNEZ, J. & MOSER, R. D. 2013 One-point statistics for turbulent wall-bounded flows at Reynolds numbers up to $\delta^+ \approx 2000$. *Phys. Fluids* **25**, 105102.
- TOWNE, A., SCHMIDT, O. T. & COLONIUS, T. 2018 Spectral proper orthogonal decomposition and its relationship to dynamic mode decomposition and resolvent analysis. *J. Fluid Mech.* **847**, 821–867.
- TSUJI, Y., FRANSSON, J. H. M., ALFREDSSON, P. H. & JOHANSSON, A. V. 2007 Pressure statistics and their scaling in high-Reynolds-number turbulent boundary layers. *J. Fluid Mech.* **585**, 1–40.
- TSUJI, YOSHIYUKI, MARUSIC, IVAN & JOHANSSON, ARNE V 2016 Amplitude modulation of pressure in turbulent boundary layer. *International Journal of Heat and Fluid Flow* **61**, 2–11.
- WILLMARTH, W. W. 1975 Pressure fluctuations beneath turbulent boundary layers. *Ann. Rev. Fluid Mech.* **7**, 13–36.
- WILLMARTH, W. W. & WOOLDRIDGE, C. E. 1962 Measurements of the fluctuating pressure at the wall beneath a thick turbulent boundary layer. *J. Fluid Mech.* **14**, 187–210.